

# Homogenization of non-rigid origami metamaterials as Kirchhoff-Love plates

Siva P. Vasudevan<sup>a</sup>, Phanisri P. Pratapa<sup>a,\*</sup>

<sup>a</sup>*Department of Civil Engineering, Indian Institute of Technology Madras, Chennai, TN 600036, India*

---

## Abstract

Origami metamaterials have gained considerable attention for their ability to control mechanical properties through folding. Consequently, there is a need to develop systematic methods for determining their effective elastic properties. This study presents an energy-based homogenization framework for non-rigid origami metamaterials, effectively linking their mechanical treatment with that of traditional materials. To account for the unique mechanics of origami systems, our framework incorporates out-of-plane curvature fields alongside the usual in-plane strain fields used for homogenizing planar lattice structures. This approach leads to a couple-stress continuum, resembling a Kirchhoff-Love plate model, to represent the homogeneous response of these lattices. We use the bar-and-hinge method to assess lattice stiffness, and validate our framework through analytical results and numerical simulations of finite lattices. Initially, we apply the framework to homogenize the well-known Miura-ori pattern. The results demonstrate the framework's ability to capture the unconventional relationship between stretching and bending Poisson's ratios in origami metamaterials. Subsequently, we extend the framework to origami lattices lacking centrosymmetry, revealing two distinct neutral surfaces corresponding to bending along two lattice directions, unlike in the Miura-ori pattern. Our framework enables the inverse design of metamaterials that can mimic the unique mechanics of origami tessellations using techniques like topology optimization.

*Keywords:* homogenization, origami metamaterials, couple-stress, Kirchhoff-Love plate, bar and hinge model, effective medium.

---

## 1. Introduction

Origami, the art of paper folding, is increasingly used to engineer novel systems with unique properties. It is applied in various fields and scales, from graphene folding (Mu et al., 2015) to deploying large space membranes (Miura, 1985; Zirbel et al., 2013). Origami also has garnered attention as metamaterials, such as those with extreme Poisson's ratios (Vasudevan and Pratapa, 2021; Liu et al., 2022), programmable stiffness (Silverberg et al., 2014), tunable thermal expansion (Boatti et al., 2017), and reprogrammable kinematics (Pratapa et al., 2021).

A number of theoretical methods are available to predict the response of origami structures (Zhu et al., 2022), including the bar and hinge model that treat these foldable sheets as enhanced three-dimensional (3D) truss systems (Schenk, 2012; Filipov et al., 2017). However, for metamaterials, the small unit cell dimensions relative to the lattice scale make detailed analysis impractical due to high computational cost. A viable alternate is to substitute the discrete model with an equivalent continuum through homogenization (Hassani and Hinton, 2012).

Various methods to find effective homogeneous medium for periodic lattice structures exist in the literature (Arabnejad and Pasini, 2013). The traditional approach involves considering only

---

\*Corresponding Author ([ppratapa@civil.iitm.ac.in](mailto:ppratapa@civil.iitm.ac.in))

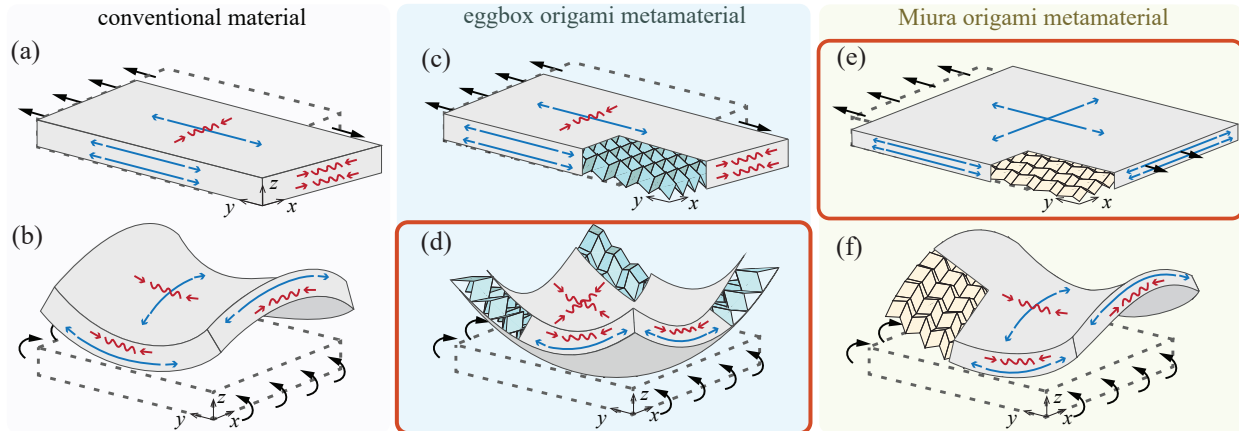


Figure 1: Illustrating the unique kinematics of origami metamaterials: contrasting Poisson effects in bending and stretching. Conventional materials with positive Poisson’s ratio in stretching (a) form a saddle shape in bending (b), while origami systems exhibit the opposite behavior. For instance, Eggbox displays a positive Poisson effect in stretching (c) but takes on a dome shape in bending (d). On the other hand, Miura-ori lattice forms a saddle shape in bending (f) but displays a negative Poisson effect in stretching (e).

in-plane strain fields based on Cauchy continuum theory (Hutchinson and Fleck, 2006; Vigliotti and Pasini, 2012). However, this approach falls short in explaining the unique mechanics of origami metamaterials. To explain, consider this: unlike conventional materials with positive Poisson’s ratios that form a saddle shape under bending (Figs. 1a, b), origami lattices exhibit contrasting behavior. For example, the Eggbox pattern displays a positive Poisson effect in stretching but forms a dome shape in bending (Figs. 1c, d), and Miura-ori lattice maintains a saddle shape in bending but exhibits a negative Poisson effect in stretching (Figs. 1e, f). This intriguing behavior extends beyond these patterns and is observed in several other origami designs (Seffen, 2012; Schenk and Guest, 2013; Wei et al., 2013; Pratapa et al., 2019; Liu et al., 2022; Nassar et al., 2022; McInerney et al., 2022). Therefore, an effective continuum for two-dimensional (2D) origami metamaterials should independently capture the out-of-plane behavior, unlike the Cauchy continuum, where the out-of-plane mechanics is directly derived from the in-plane elasticity coefficients.

Prior studies aimed at determining the homogeneous behavior of origami metamaterials have commonly assumed that the panels are axially rigid (Evans et al., 2015; Nassar et al., 2017, 2022). This assumption confines the lattice deformation to crease folding and panel bending. However, this constraint transforms the lattice into a mechanism, posing challenges in applying the extensive homogenization tools used in other lattice systems, such as cellular materials, to origami. Other related research has not primarily focused on deriving the effective properties of origami lattices; instead, they have considered these systems either as folded cores in sandwich panels along with other structural elements (Lebée and Sab, 2012) or as frame lattices with fully rigid joints that prevent relative rotations between the panels (Abdoul-Anziz and Seppecher, 2018).

To fully regard origami lattices as metamaterials, we require methods akin to those used for homogenizing cellular materials. This approach would align the treatment of origami metamaterials more closely with conventional materials, and aid in the inverse design of architected metamaterials that mimic the unique mechanics of origami tessellations through techniques like topology optimization. Design of such structures serves at least two key purposes: firstly, it may provide valuable insights into the underlying mechanisms of the unique behavior of origami, and secondly, it unveils a novel class of lattice metamaterials with distinct Poisson’s ratio values in stretching and bending.

Based on the above motivation, we propose an energy-based homogenization framework for non-rigid origami metamaterials. This framework incorporates out-of-plane curvature fields, in addition to the in-plane strain fields typically considered in traditional homogenization methods. The introduction of the curvature fields results in a generalized continua, surpassing the confines of Cauchy’s theory, to describe the homogeneous response of planar origami lattices. Specifically, we homogenize non-rigid planar origami metamaterials as couple-stress continua (Toupin, 1962; Thai et al., 2017) by including strain gradients in the form of curvature fields. The resulting effective medium is directly analogous to the popular Kirchhoff-Love theory for 2D plates, where linear and rotational displacements are the independent variables (Srinivasa and Reddy, 2017). But a fundamental difference is that the Kirchhoff-Love models are reduced dimensional approximations for a 3D classical continuum member, while couple-stress is a different continuum model in itself. Nevertheless, homogenized models for 2D origami lattices are described more often as a Kirchhoff-Love plate (Buannic et al., 2003; Khakalo and Niiranen, 2020) and we stay consistent with that description. For structural analysis and energy calculations, we adopt a matrix-based approach akin to Vigliotti and Pasini (2012).

The outline of the paper is as follows. We begin by discussing the homogenization of a simplified one-dimensional (1D) zigzag lattice in Section 2. This serves as a foundational step in understanding our proposed framework for origami lattices. In Section 3, we present the framework to homogenize a generalized 2D origami pattern, where we estimate the effective elasticity matrix and physical elastic constants. In Section 4, we apply the framework to the well-known Miura-ori pattern and validate it through analytical and numerical results. Finally, in Section 5, we discuss on non-centrosymmetric origami lattices, where we show the presence of two distinct neutral surfaces for bending in each lattice direction. We conclude the paper with a summary of our findings and provide suggestions for future research.

## 2. Homogenization of a Simplified 1D Foldable Lattice

In this section, we introduce the framework by homogenizing a simplified 1D zigzag foldable lattice (Fig. 2). This lattice is geometrically simpler than a more complex 2D origami lattice but still exhibits many of the same characteristics. By solving the 1D problem, we can clearly describe the proposed framework and prepare for its application to 2D origami lattices in subsequent sections.

### 2.1. Description of geometry

The infinite 1D zigzag lattice consists of axial bars connected by rotational springs at their ends (Fig. 2a). To determine the effective properties of the entire lattice, we focus on a single unit cell while considering the effects of periodic boundary conditions. This unit cell (Fig. 2b) comprises two bars (1 – 2 and 2 – 3) and two rotational hinges (at nodes 2 and 3). To correctly capture the structural deformation, it is necessary to consider nodes 3 and 4 (which correspond to the neighboring cell) in addition to nodes 1 and 2. This is so because, node 3’s displacement affects the extension of bar 2 – 3, and node 4’s displacement deforms the flexural spring at node 3. However, since node 4 is not connected to any structural member of the unit cell, we introduce a virtual bar with zero axial stiffness that connects nodes 3 and 4 (depicted as a dotted line in Fig. 2b).

Nodes 1 and 2 are considered “independent” as they are just sufficient to create the entire lattice through periodic translation along the lattice vector  $a_x \hat{e}_x$ , where  $\hat{e}_x$  is a unit vector along the  $x$ -direction. Nodes 3 and 4, on the other hand, are referred to as “dependent” nodes. In Fig. 2, solid and hollow circles differentiate between independent and dependent nodes. From the geometric periodicity of the lattice, the position of any node  $i \in \{1, 2, 3, 4\}$  is related to the position

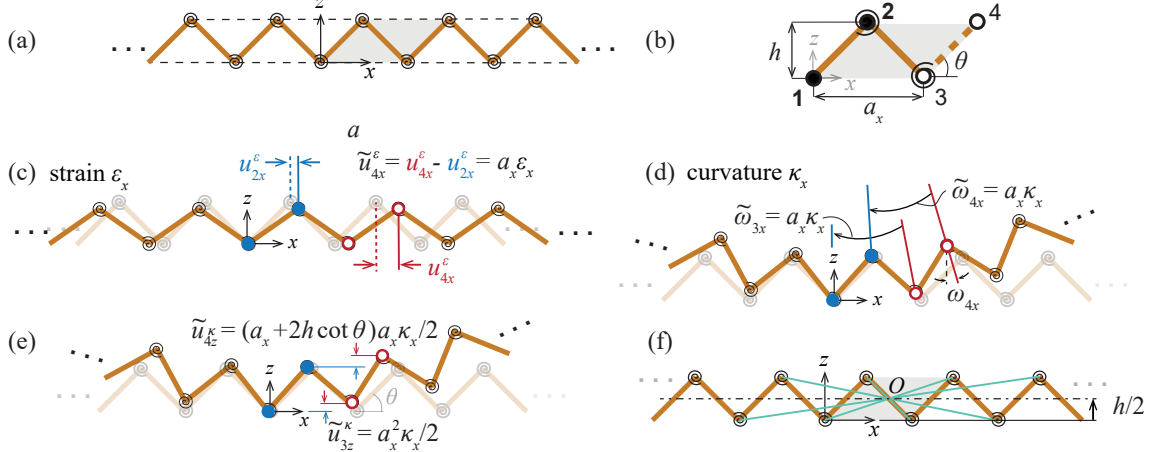


Figure 2: A simple zigzag foldable lattice having features of origami. (a) The 1D lattice consists of rigid bars connected through rotational hinges at the ends. (b) A unit cell comprises two bars and two rotational hinges. (c) Under a global strain  $\epsilon_x$ , displacements at nodes 2 and 4 are indicated. (d) Under a global curvature  $\kappa_x$ , rotations at nodes 3 and 4 relative to nodes 1 and 2 are depicted; (e) these rotations are expressed as displacements at nodes 3 and 4. (f) The lattice has an inversion symmetry about point  $O$ .

of an independent node  $j \in \{1, 2\}$ . We define this relation  $P$  as a set of ordered pairs:

$$P = \{(i, j) \in \mathcal{W} \times \mathcal{W}_0 : \mathbf{r}(i) = \mathbf{r}(j) + s_x a_x \hat{\mathbf{e}}_x, s_x \in \mathbb{Z}\}, \quad (1)$$

where  $\mathcal{W} = \{1, 2, 3, 4\}$  and  $\mathcal{W}_0 = \{1, 2\}$  are the set of all nodes and only independent nodes, respectively;  $\mathbf{r}(i)$  and  $\mathbf{r}(j)$  are the position vectors of nodes  $i$  and  $j$ , respectively. In the roster form,  $P$  is given as

$$P = \{(1, 1), (2, 2), (3, 1), (4, 2)\}. \quad (2)$$

Let a macroscopic deformation field be imposed on this lattice (Section S1 of the supplementary material discusses more on a macroscopic field in periodic lattices). Under this global field, we represent the displacements of all four nodes by  $\mathbf{u} = (\mathbf{u}_i)_{i \in \mathcal{W}}$ , and the displacements of only independent nodes as  $\mathbf{u}_0 = (\mathbf{u}_j)_{j \in \mathcal{W}_0}$ . Here,  $\mathbf{u}_{i[2 \times 1]}$  contains the  $x$  and  $z$  displacement degrees of freedom (*dofs*) of the  $i^{\text{th}}$  node. Variables  $\mathbf{u}$  and  $\mathbf{u}_0$  can be explicitly written as

$$\mathbf{u}_{[8 \times 1]} = [\mathbf{u}_1 \quad \mathbf{u}_2 \quad \mathbf{u}_3 \quad \mathbf{u}_4]^T, \quad \mathbf{u}_0_{[4 \times 1]} = [\mathbf{u}_1 \quad \mathbf{u}_2]^T. \quad (3)$$

We can now define the relative displacement of each node  $i$  with respect to its independent node (defined through the periodicity relation  $P$ ) as  $\tilde{\mathbf{u}} = (\tilde{\mathbf{u}}_i)_{i \in \mathcal{W}}$ . That is,

$$\tilde{\mathbf{u}}_i = \mathbf{u}_i - \mathbf{u}_j; \quad (i, j) \in P. \quad (4)$$

Note that in the above equation, although  $\tilde{\mathbf{u}}_i$  is relating to nodes  $i$  and  $j$ , it is denoted with a subscript of only  $i$ , as  $j$  is not a separate variable but is known for every  $i \in \mathcal{W}$  through the periodicity relation  $P$ . The relative displacement vector  $\tilde{\mathbf{u}}_i$  can be shown as

$$\begin{aligned} \tilde{\mathbf{u}}_{[8 \times 1]} &= [\tilde{\mathbf{u}}_1 \quad \tilde{\mathbf{u}}_2 \quad \tilde{\mathbf{u}}_3 \quad \tilde{\mathbf{u}}_4]^T \\ &= [\mathbf{u}_1 - \mathbf{u}_1 \quad \mathbf{u}_2 - \mathbf{u}_2 \quad \mathbf{u}_3 - \mathbf{u}_1 \quad \mathbf{u}_4 - \mathbf{u}_2]^T. \end{aligned} \quad (5)$$

After using Eqn. 3, the above equation can be rearranged to the following.

$$\mathbf{u} = \mathbf{P}\mathbf{u}_0 + \tilde{\mathbf{u}}, \quad (6)$$

where  $\mathbf{P}$  is the Boolean matrix of relation  $P$  and is given by

$$\mathbf{P}_{ij} = \begin{cases} \mathbf{I}_{2 \times 2} & \forall (i, j) \in P \\ \mathbf{O}_{2 \times 2} & \text{for other values of } (i, j) \in \mathcal{W} \times \mathcal{W}_0, \end{cases} \quad (7)$$

where  $\mathbf{I}_{2 \times 2}$  and  $\mathbf{O}_{2 \times 2}$  are identity and null matrices of size  $2 \times 2$ , respectively. When expanded,  $\mathbf{P}$  takes the following form.

$$\mathbf{P}_{[8 \times 4]} = \begin{bmatrix} \mathbf{I}_{2 \times 2} & \mathbf{O}_{2 \times 2} \\ \mathbf{O}_{2 \times 2} & \mathbf{I}_{2 \times 2} \\ \mathbf{I}_{2 \times 2} & \mathbf{O}_{2 \times 2} \\ \mathbf{O}_{2 \times 2} & \mathbf{I}_{2 \times 2} \end{bmatrix}. \quad (8)$$

Through Eqn. 6, we decompose the displacement field  $\mathbf{u}$  of the unit cell into the displacement of independent nodes  $\mathbf{u}_0$  and the relative displacements  $\tilde{\mathbf{u}}$ . In the following subsections, we solve for these two parts under certain macroscopic deformation fields.

## 2.2. Periodicity of displacements

Macroscopic deformations, like uniform expansion, reflect as relative displacements between unit cell boundaries at the microscale (refer to Section 1 of supplementary material). In this section, we find these relative displacements  $\tilde{\mathbf{u}}$  caused by two specific fields: axial strain  $\epsilon_x$  and curvature  $\kappa_x$  along the lattice direction  $x$ .

The displacement of a node  $i$  at position  $(x_i, z_i)$  relative to its corresponding independent node at  $(x_j, z_j)$  due to a global strain  $\epsilon_x$  is given by

$$\tilde{\mathbf{u}}_i^\epsilon = \begin{bmatrix} \tilde{x}_i \\ 0 \end{bmatrix} \epsilon_x, \quad (9)$$

where  $\tilde{x}_i = x_i - x_j$  represents the relative  $x$  position of node  $i$  with reference to its independent node. Note that  $\tilde{x}_i$  is constant and equals  $a_x$  (see Fig. 2b, 2c). Despite this, we maintain the expression in terms of nodal coordinates for convenience in describing other macroscopic fields. Similarly, when a curvature field  $\kappa_x$  is imposed (Fig. 2d), the relative nodal rotation  $\tilde{\omega}_i$  is expressed as

$$\tilde{\omega}_i = \tilde{x}_i \kappa_x, \quad (10)$$

where  $\tilde{\omega}_i = \omega_i - \omega_j$  is found as the difference in rotations of node  $i$  and its corresponding independent node  $j$ . These rotations can be converted to displacements using geometry (Fig. 2e), resulting in:

$$\tilde{\mathbf{u}}_i^\kappa = \begin{bmatrix} (h^* - z_i)\omega_i - (h^* - z_j)\omega_j \\ 0.5\kappa_x(x_i^2 - x_j^2) \end{bmatrix}, \quad (11)$$

where  $h^*$  is the height where no relative horizontal displacements between the unit cell boundaries occur due to  $\kappa_x$ . Setting the value of  $h^*$  to the mid-height<sup>1</sup>  $h/2$  and recognizing that  $z_i = z_j$ , it becomes

$$\tilde{\mathbf{u}}_i^\kappa = \frac{1}{2}\tilde{x}_i \begin{bmatrix} h - 2z_i \\ x_i + x_j \end{bmatrix} \kappa_x. \quad (12)$$

---

<sup>1</sup>This choice is unsurprising as the neutral axis of this lattice is in fact at  $h^* = h/2$ . However, for more complex lattices,  $h^*$  may still be taken at  $h/2$  for simplicity. Such cases are discussed later in this paper.

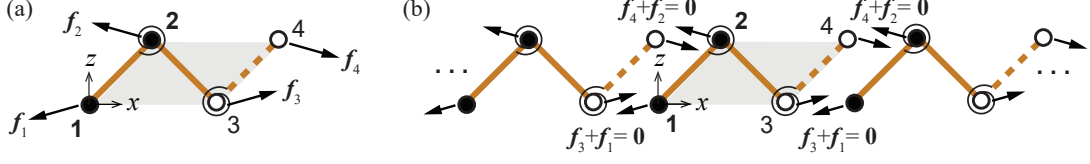


Figure 3: (a) Nodal forces on the zigzag unit cell. (b) Illustration of force periodicity

When considering the effects of both strain and curvature fields, the relative displacement  $\tilde{\mathbf{u}} = \tilde{\mathbf{u}}^\epsilon + \tilde{\mathbf{u}}^\kappa$  becomes a linear function of the macroscopic field  $\mathbf{e} = [\epsilon_x \ \kappa_x]^\top$  (combining Eqns. 9 and 12):

$$\tilde{\mathbf{u}}_{[8 \times 1]} = \mathbf{G}_{\tilde{\mathbf{u}}}_{[8 \times 2]} \mathbf{e}_{[2 \times 1]}, \quad (13)$$

where  $\mathbf{G}_{\tilde{\mathbf{u}}}_{[8 \times 2]}$  is a matrix of geometrical quantities. By substituting nodal coordinates in terms of  $a_x, h$  and  $\theta$  (Fig. 2b),  $\mathbf{G}_{\tilde{\mathbf{u}}}$  is expressed as

$$\mathbf{G}_{\tilde{\mathbf{u}}}_{[8 \times 2]} = \frac{1}{2} a_x \begin{bmatrix} 0 & 0 & 0 & 0 & 2 & 0 & 2 & 0 \\ 0 & 0 & 0 & 0 & h & a_x & -h & a_x + 2h \cot \theta \end{bmatrix}^\top. \quad (14)$$

Eqn. 13 establishes a relationship between  $\tilde{\mathbf{u}}$  and  $\mathbf{e}$ . The next step is to find a similar expression for  $\mathbf{u}_0$ . To achieve this, we apply force periodicity and equilibrium constraints on the unit cell.

### 2.3. Periodicity of forces

Macroscopic deformation fields induce forces at the lattice nodes. These forces, although internal at the global scale (Fig. 3b), become external when the unit cell is analyzed separately (Fig. 3a). Let  $\mathbf{f} = (\mathbf{f}_i)_{i \in \mathcal{W}}$  denote such nodal forces in the unit cell due to the combined action of  $\epsilon$  and  $\kappa$ :

$$\mathbf{f}_{[8 \times 1]} = [\mathbf{f}_1 \ \mathbf{f}_2 \ \mathbf{f}_3 \ \mathbf{f}_4]^\top,$$

where  $\mathbf{f}_{i[2 \times 1]}$  contains the  $x$  and  $z$  force components at  $i^{\text{th}}$  node. A force-displacement relation can be established through the stiffness matrix  $\mathbf{K}_{[8 \times 8]}$  as

$$\mathbf{f}_{[8 \times 1]} = \mathbf{K}_{[8 \times 8]} \mathbf{u}_{[8 \times 1]}. \quad (15)$$

For the computation of the stiffness matrix, one can use well-established structural analysis methods, as detailed in Section S2 of the supplementary material. Nodal forces also adhere to periodicity constraints to ensure net forces vanish in an infinite lattice under macroscopic deformation (Fig. 3b):

$$\mathbf{f}_1 + \mathbf{f}_3 = 0, \quad \mathbf{f}_2 + \mathbf{f}_4 = 0. \quad (16)$$

These constraints can be compactly expressed using the periodicity matrix  $\mathbf{P}$  (given in Eqn. 8) as

$$\mathbf{P}_{[8 \times 4]}^\top \mathbf{f}_{[8 \times 1]} = \mathbf{O}_{[4 \times 1]}. \quad (17)$$

Solving Eqns. 6, 13, 15 and 17, we get find the expression for  $\mathbf{u}_0$  as

$$\mathbf{u}_0_{[4 \times 1]} = \mathbf{G}_{\mathbf{u}_0}_{[4 \times 2]} \mathbf{e}_{[2 \times 1]}, \text{ where} \quad (18a)$$

$$\mathbf{G}_{\mathbf{u}_0} = -(\mathbf{P}^\top \mathbf{K} \mathbf{P})^\dagger (\mathbf{P}^\top \mathbf{K} \mathbf{G}_{\tilde{\mathbf{u}}}), \quad (18b)$$

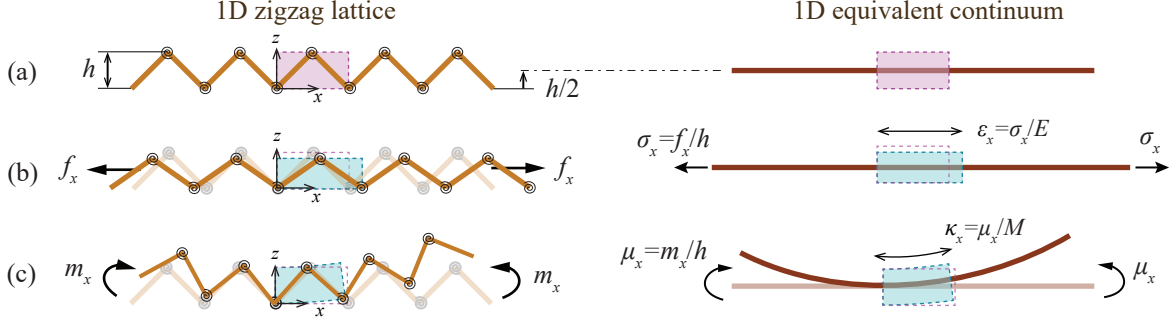


Figure 4: Homogenization of the 1D zigzag lattice: (a) The effective medium represents deformation at mid-height for stretching and bending. (b) Strain  $\epsilon_x = \sigma_x/E$  results from uniform stretching, as the ratio of distributed force (“force-stress”) to Young’s modulus. (c) Curvature  $\kappa_x = \mu_x/M$  is the ratio of distributed moment (“couple-stress”) to the bending modulus.

where  $(\cdot)^\dagger$  denotes the Moore-Penrose pseudo-inverse operator; a direct inverse is not possible as the unit cell is unconstrained (without any boundary conditions) in Eqn. 15, and so the stiffness matrix  $\mathbf{K}$  would have a non-empty null space.

It is notable in the above equation that the displacement  $\mathbf{u}_0$  of the independent nodes depends on both geometry (from  $\mathbf{P}$  and  $\mathbf{G}_{\tilde{\mathbf{u}}}$ ) and material factors (from  $\mathbf{K}$ ) of the lattice, unlike the relative displacements  $\tilde{\mathbf{u}}$  that depend just on geometric factors (see Eqn. 14). Substituting Eqns. 13 and 18 into Eqn. 6, we find

$$\mathbf{u}_{[8 \times 1]} = \mathbf{G}_{\mathbf{u}[8 \times 2]} \mathbf{e}_{[2 \times 1]}, \text{ where} \quad (19a)$$

$$\mathbf{G}_{\mathbf{u}} = \mathbf{P} \mathbf{G}_{\mathbf{u}_0} + \mathbf{G}_{\tilde{\mathbf{u}}}. \quad (19b)$$

This expression for  $\mathbf{u}$  in terms of  $\mathbf{e}$  allows us to calculate the elastic energy density stored in the lattice. We will compare this energy with that of an effective homogeneous medium subjected to the same deformation field  $\mathbf{e}$ . Through this comparison, we find an equivalent medium for the lattice.

#### 2.4. Effective continuum model

Elastic energy density  $U$  stored in the lattice is estimated as

$$\begin{aligned} U &= \frac{1}{ha_x} \left( \frac{1}{2} \mathbf{f}^T \mathbf{u} \right) \\ &= \frac{1}{2} \mathbf{e}^T \left( \frac{1}{ha_x} \mathbf{G}_{\mathbf{u}}^T \mathbf{K} \mathbf{G}_{\mathbf{u}} \right) \mathbf{e}, \end{aligned} \quad (20)$$

where we have used  $\mathbf{f} = \mathbf{K} \mathbf{u}$  (Eqn. 15) and  $\mathbf{u} = \mathbf{G}_{\mathbf{u}} \mathbf{e}$  (Eqn. 19a). To model the lattice as an equivalent continuum, we need to compare this energy density with that of a beam-like medium subjected to the same macroscopic field. The comparison is with a beam-like medium and not with a bar-like medium (with only axial stiffness), as the elastic energy should depend not only on strains but also on curvatures. Such a medium falls outside the regime of Cauchy continuum theory, where only strain terms appear in describing elastic energy. In a second gradient-based couple-stress theory, the expression for elastic energy contains both strains and curvatures, and is well suited for modeling the 1D zigzag lattice as an equivalent homogeneous medium. The elastic

energy density  $U_{\text{eff}}$  of such an effective medium is expressed as

$$U_{\text{eff}} = \frac{1}{2} \mathbf{e}^T \mathbf{C} \mathbf{e} \quad (21a)$$

$$= \frac{1}{2} \begin{bmatrix} \epsilon_x & \kappa_x \end{bmatrix} \begin{bmatrix} A & B \\ B & D \end{bmatrix} \begin{bmatrix} \epsilon_x \\ \kappa_x \end{bmatrix}, \quad (21b)$$

where  $\mathbf{C}_{[2 \times 2]}$  is the effective elasticity matrix with scalar components  $\mathbf{A}$ ,  $\mathbf{B}$  and  $\mathbf{D}$ . Terms  $\mathbf{A}$  and  $\mathbf{D}$  are, respectively, Young's modulus  $E_x$  and the bending modulus  $M_x$  of the continuum that represent the stiffness against stretching and bending fields; term  $\mathbf{B}$  indicates the extent of coupling present between the axial and bending behavior. Since the zigzag structure has an inversion symmetry, commonly referred to as *centrosymmetry*, about a point located mid-height (refer to Fig. 2f), axial and bending behaviors are decoupled with  $\mathbf{B} = 0$ .

In lattice structures, *centrosymmetry* operation is an inversion through a point in the structure so that any element at a position  $(x, y, z)$  with reference to that point is paired with an identical element at  $(-x, -y, -z)$ . On existence, such a point about which this inversion occurs is known as the center of symmetry. The unit cell (and the entire lattice) remains invariant to inversion about that central point (Tilley, 2020; Cui et al., 2022, 2023). The centrosymmetry operator is often represented as  $\bar{1}$ , and its transformation matrix, that transforms the old to the new coordinate bases, is simply the negative of identity matrix. We refer a structure to be *centrosymmetric* if it is unaffected by the centrosymmetry operation.

By equating the expressions for the elastic energy density of the lattice (Eqn. 20) with that of the homogeneous medium (Eqn. 21a), we find that

$$\mathbf{C} = \frac{1}{ha_x} \mathbf{G}_u^T \mathbf{K} \mathbf{G}_u. \quad (22)$$

After using the expressions for  $\mathbf{G}_{\bar{u}}$  (Eqn. 14),  $\mathbf{G}_{u_0}$  (Eqn. 18),  $\mathbf{G}_u$  (Eqn. 19b) and  $\mathbf{K}$  (Section S2 of supplementary material), we find a closed form solution for  $\mathbf{C}$  and express for a special case when all bars are of equal lengths  $l$  and subtend angle  $\theta$  with horizontal:

$$\mathbf{C} = \begin{bmatrix} \frac{4k_h k_s \cot \theta}{k_s h^2 - 4k_h \cos^2 \theta} & 0 \\ 0 & k_h \cot \theta \end{bmatrix}, \quad (23)$$

where  $k_s$  and  $k_h$  are the bars' axial stiffness and the hinges' rotational stiffness, respectively. The effective elasticity matrix  $\mathbf{C}$  provides a description of how the lattice responds to applied loads through the constitutive relation:

$$\boldsymbol{\tau}_{[2 \times 1]} = \mathbf{C}_{[2 \times 2]} \mathbf{e}_{[2 \times 1]}, \quad (24)$$

where  $\boldsymbol{\tau} = [\sigma_x \ \mu_x]^T$  is the stress field containing force-stress  $\sigma_x$  and couple-stress  $\mu_x$ .

To get a feel for the effective moduli  $E_x$  and  $M_x$  of the zigzag lattice, we assign these numerical values: bar length  $l = 50\text{mm}$ , bars' axial stiffness  $k_s = 100\text{N/mm}$ , rotational hinge stiffness<sup>2</sup>  $k_h = 1\text{Nmm/rad}$ . From geometry, length of lattice vector  $a_x = 100 \cos \theta$  mm and height  $h = 50 \sin \theta$  mm. Using these values in Eqn. 23, we find  $E_x$  and  $M_x$  and plot their variation with folding angle  $\theta$  in Fig. 5. Notably, the bending modulus  $M_x$  is highest at the deployed state and lowest at the fully

---

<sup>2</sup>A small value for the rotational hinge stiffness comparative to bars' stiffness mimics the compliant folding nature of origami structures.

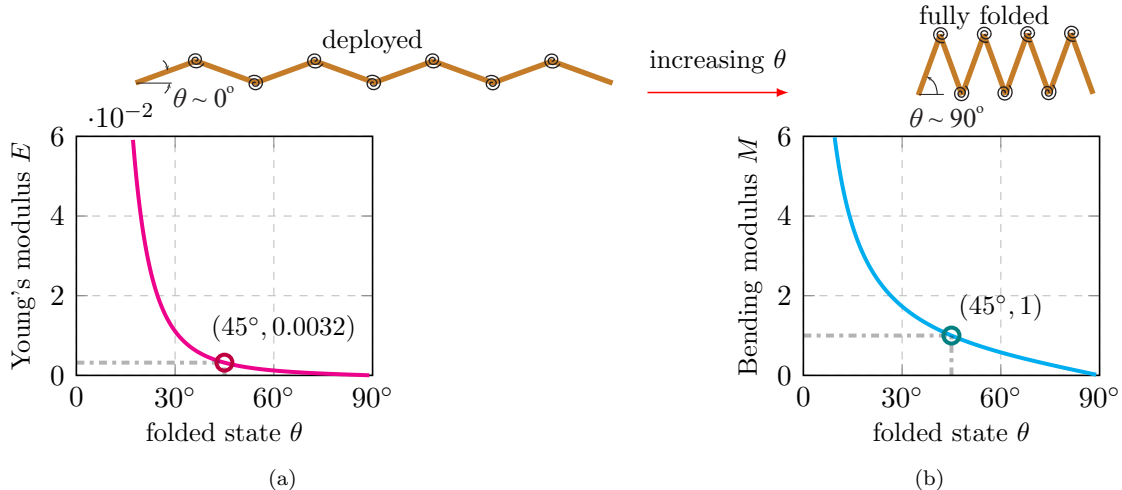


Figure 5: Variation of (a) Young’s modulus  $E$  and (b) bending modulus  $M$  of the zigzag lattice with folding angle  $\theta$ .

Table 1: Values taken for zigzag lattice parameters and the effective moduli obtained from homogenization.

Considered values					Homogenized result		
$\theta$ (deg)	$a_x$ (mm)	$h$ (mm)	$k_s$ (N/mm)	$k_h$ (Nmm/rad)	$E_x$ (N/mm)	$M_x$ (Nmm)	$M_x/(E_x h^2/12)$
45°	$50\sqrt{2}$	$25\sqrt{2}$	100	1	$3.2 \times 10^{-3}$	1	3

folded state, contrary to the intuitive expectation that “thicker” state (with greater  $h$ ) has a higher resistance to bending. The reasoning goes as follows. For an applied moment  $m_x$  (Fig. 4c), end rotations remain the same at all states (because  $k_h$  is constant), which results in different curvatures  $\kappa_x$  at different states. Curvatures, being the gradient of rotations, are lowest at the deployed state, and highest at the fully folded state. Consequently,  $m_x/\kappa_x$  decreases from deployed to the fully folded state. Furthermore, the reduction in lattice height  $h$  with folding further strengthens this decreasing trend of  $M_x = m_x/(h\kappa_x)$  in Fig. 5.

At  $\theta = 45^\circ$  (marked in Fig. 5), we find that  $E_x = 0.0032$  (N/mm) and  $M_x = 1$  (Nmm). It is evident that the bending modulus  $M_x = 1$  (Nmm) cannot be straightforwardly predicted from the Young’s modulus  $E_x = 0.0032$  (N/mm) using Euler’s beam theory with the formula  $M_x = Eh^2/12$  (also refer to Table 1 and Eqn. 23). This result highlights the independence of the lattice’s out-of-plane behavior from its in-plane response. Consequently, both in-plane and out-of-plane deformation fields are necessary for comprehensive characterization of this lattice. Based on this insight, we consider both in-plane and out-of-plane fields to characterize origami metamaterials in the following section.

### 3. Homogenization Framework for Planar Origami Metamaterials

This section presents the homogenization framework for analyzing planar non-rigid origami metamaterials. Essentially, these are 2D lattices within a 3D Euclidean space. We consider a fairly generic origami pattern with quadrilateral panels shown in Fig. 6a to describe the geometric and structural modeling framework for homogenization. The pattern is a combination of square twist and Miura-ori patterns (Liu et al., 2016). We begin by outlining the geometric characteristics of the structure and analyzing the unit cell under periodic constraints for different deformation fields. Then, we calculate the elasticity matrix of the effective medium using the principle of energy

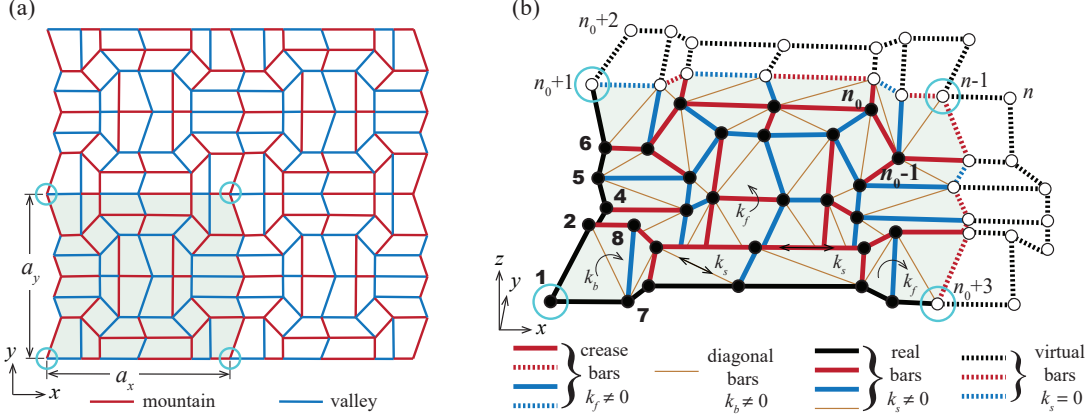


Figure 6: An origami pattern. (a) Crease pattern for the origami structure in its developed (fully unfolded) state. (b) A bar and hinge model representation for the unit cell of the origami lattice in a partially folded state. Here the panels are triangulated by providing bars along one of the diagonals in addition to crease locations.

equivalence. Finally, we examine the physical significance of the metamaterial constants obtained from the elasticity matrix.

### 3.1. Description of geometry

Origami structures can be modeled in various ways (Zhu et al., 2022). In this study, we adopt a simplified and computationally efficient bar-and-hinge model to derive the stiffness matrix  $\mathbf{K}$  the origami unit cell (Filipov et al., 2017). Nonetheless, we emphasize that the proposed homogenization framework is versatile and can be applied to other structural models, including a more detailed finite element model, estimating the stiffness matrix  $\mathbf{K}$  of the unit cell. For the sake of simplicity and to illustrate the concept, here we opt to demonstrate it using the basic N4B5 bar-and-hinge model. In this model, the cell is considered as an enhanced truss by assigning bars along the creases and shorter panel diagonals, and taking finite rotational hinge stiffness for crease folding and panel bending (Fig. 6b). In Fig. 6b, solid lines represent bars with axial stiffness, while dashed lines denote virtual bars without axial stiffness. Red (mountain fold) and blue (valley fold) indicate hinge stiffness for crease folding, and thin brown lines on panel diagonals represent hinge stiffness for panel bending. No rotational hinges are applied about the black bars. The specific choice of the virtual bars and black bars described above ensures that the elastic energy of the unit cell is fully accounted for.

The unit cell contains  $n_0$  independent nodes (solid circles in Fig. 6b) of the total  $n$  nodes. Dependent nodes are shown as hollow circles and numbered from  $n_0 + 1$  to  $n$ . Some of these dependent nodes, such as  $n_0 + 2, n - 1, n$ , etc., although not connected to any bar with axial stiffness, are still needed to account for rotational spring deformation about the bars at the unit cell boundary (red and blue dashed lines in Fig. 6b). Virtual bars of zero axial stiffness (dashed lines in Fig. 6b) are introduced to model these nodes. The lattice exhibits translational periodicity with lattice vectors  $\{a_x \hat{e}_x, a_y \hat{e}_y\}$ . The position of every node  $i \in \mathcal{W} = \{1, 2, 3, \dots, n\}$  is therefore related to an independent node  $j \in \mathcal{W}_0 = \{1, 2, 3, \dots, n_0\}$  through a periodicity relation  $P$ , akin to the 1D case shown in Eqn. 1:

$$P = \{(i, j) \in \mathcal{W} \times \mathcal{W}_0 : \mathbf{r}(i) = \mathbf{r}(j) + s_x a_x \hat{e}_x + s_y a_y \hat{e}_y, s_x \in \mathbb{Z}, s_y \in \mathbb{Z}\}, \quad (25)$$

where  $\mathbf{r}(i)$  and  $\mathbf{r}(j)$  are the position vectors of nodes  $i$  and  $j$ . Some representative elements in  $P$  include  $(1, 1), (n_0 + 1, 1), (n_0 + 3, 1), (n - 1, 1)$  corresponding to  $j = 1$  (representing the corners of

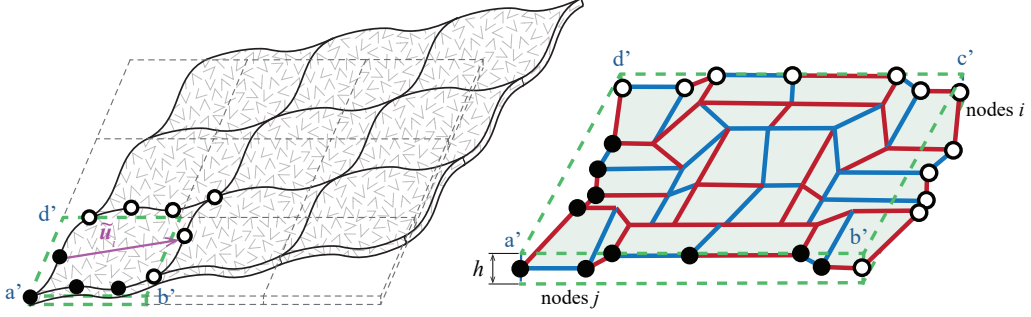


Figure 7: Illustration of lattice deformation under a uniform macroscopic field – although the deformation within the unit cell could be non-uniform due to material or geometric inhomogeneity, the relative displacements  $\tilde{\mathbf{u}}_i$  are uniform across the lattice.

the unit cell, highlighted in Fig. 6). The Boolean matrix  $\mathbf{P}_{[3n \times 3n_0]}$  of the periodic relation takes the following form.

$$\mathbf{P}_{ij} = \begin{cases} \mathbf{I}_{3 \times 3} & \forall (i, j) \in P \\ \mathbf{O}_{3 \times 3} & \text{for other values of } (i, j) \in \mathcal{W} \times \mathcal{W}_0, \end{cases} \quad (26)$$

where  $\mathbf{I}_{3 \times 3}$  and  $\mathbf{O}_{3 \times 3}$  are unity and null matrices of size  $3 \times 3$ , respectively.

Nodal displacements of all  $n$  nodes are contained in  $\mathbf{u}_{[3n \times 1]} = (\mathbf{u}_i)_{i \in \mathcal{W}}$ , and the displacements of  $n_0$  independent nodes are separately taken in  $\mathbf{u}_0_{[3n_0 \times 1]} = (\mathbf{u}_j)_{j \in \mathcal{W}_0}$ , where  $\mathbf{u}_i_{[3 \times 1]}$  has the  $x, y, z$  translational *dofs* of the  $i^{\text{th}}$  node. The relative displacement of each node relative to its respective independent node is contained in  $\tilde{\mathbf{u}}_{[3n \times 1]}$ . In what follows in this section, we find the unknown nodal displacements  $\mathbf{u}$  resulting from the macroscopic deformation field.

### 3.2. Periodicity of displacements

A uniform global deformation can lead to complex displacements within a unit cell (see Fig. 7). However, the relative displacements between the cell boundaries remain uniform across the lattice and can be determined through geometric periodicity, akin to the procedure outlined in Section 2.2.

To characterize the in-plane behavior of the lattice, we consider three strain fields:  $\epsilon_x, \epsilon_y$ , and  $2\epsilon_{xy}$ . These fields correspond to axial stretching along the  $x$  and  $y$  directions and symmetric shear in the  $xy$  plane, as shown in Figs. 8a,b,c. To characterize the out-of-plane behavior, we consider three curvature fields:  $\kappa_x, \kappa_y$ , and  $2\kappa_{xy}$ . These fields are analogous to the in-plane fields and correspond to bending *along* the  $x$  and  $y$  directions and twisting of the  $xy$  plane, as depicted in Figs. 8d,e,f. These out-of-plane fields are crucial for capturing the unique behavior of origami metamaterials, such as the equal and opposite Poisson's ratio in stretching and bending (refer to Fig. 1).

Relative displacements  $\tilde{\mathbf{u}}^\epsilon$  at each node  $i$  due to the strain fields  $\epsilon_x, \epsilon_y$  and  $2\epsilon_{xy}$  can be expressed as

$$\tilde{\mathbf{u}}_i^\epsilon = \begin{bmatrix} \tilde{x}_i & 0 & \tilde{y}_i/2 \\ 0 & \tilde{y}_i & \tilde{x}_i/2 \\ 0 & 0 & 0 \end{bmatrix} \begin{bmatrix} \epsilon_x \\ \epsilon_y \\ 2\epsilon_{xy} \end{bmatrix}, \quad (27)$$

where  $(x_i, y_i, z_i)$  are the coordinates of node  $i$ , and  $\tilde{x}_i = x_i - x_j, \tilde{y}_i = y_i - y_j$  are the  $x, y$  coordinates of node  $i$  with reference to its independent node. Under curvature fields  $\kappa_x, \kappa_y$  and  $2\kappa_{xy}$ , relative

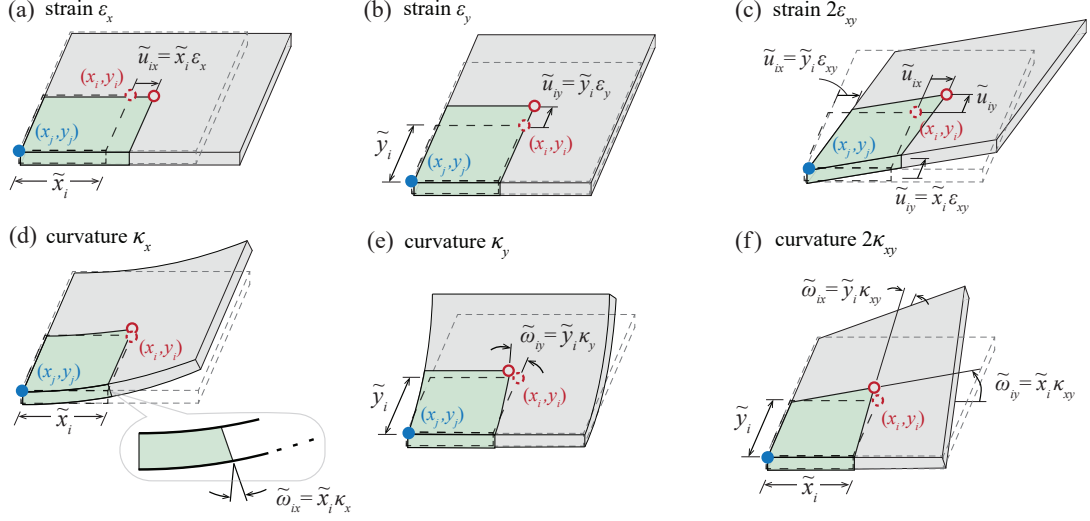


Figure 8: Illustration of the six macroscopic fields that characterize the homogeneous behavior of an origami unit cell (marked as green color). Although unit cell deformations can be non-uniform, as in Fig. 7, we depict them uniform to focus on the global field. (a),(b),(c) Relative displacements between nodes  $i$  (red hollow circle) and  $j$  (blue solid circle) due to in-plane strain fields  $\epsilon_x$ ,  $\epsilon_y$  and  $2\epsilon_{xy}$ . (d),(e),(f) Out-of-plane curvature fields  $\kappa_x$ ,  $\kappa_y$  and  $2\kappa_{xy}$  cause a relative rotation between nodes  $i$  and  $j$ .

rotations  $\tilde{\omega}^\kappa$  along  $x$ - and  $y$ -directions at node  $i$  take a similar form:

$$\tilde{\omega}_i^\kappa = \begin{bmatrix} \tilde{x}_i & 0 & \tilde{y}_i/2 \\ 0 & \tilde{y}_i & \tilde{x}_i/2 \end{bmatrix} \begin{bmatrix} \kappa_x \\ \kappa_y \\ 2\kappa_{xy} \end{bmatrix}, \quad (28)$$

These relative rotations, when expressed in terms of displacements, become

$$\tilde{\mathbf{u}}_i^\kappa = \frac{1}{2} \begin{bmatrix} \tilde{x}_i(h-2z_i) & 0 & \tilde{y}_i(h-2z_i)/2 \\ 0 & \tilde{y}_i(h-2z_i) & \tilde{x}_i(h-2z_i)/2 \\ \tilde{x}_i(x_i+x_j) & \tilde{y}_i(y_i+y_j) & x_i y_i - x_j y_j \end{bmatrix} \begin{bmatrix} \kappa_x \\ \kappa_y \\ 2\kappa_{xy} \end{bmatrix}. \quad (29)$$

By taking contributions from strain and curvature fields (in Eqns. 27 and 29), we find  $\tilde{\mathbf{u}}_{[3n \times 1]} = \tilde{\mathbf{u}}^\epsilon + \tilde{\mathbf{u}}^\kappa$  to be related to the macroscopic field  $\mathbf{e}_{[6 \times 1]} = [\boldsymbol{\epsilon} \ \boldsymbol{\kappa}]^T = [\epsilon_x \ \epsilon_y \ 2\epsilon_{xy} \ \kappa_x \ \kappa_y \ 2\kappa_{xy}]^T$  through a linear function  $\mathbf{G}_{\tilde{\mathbf{u}}[3n \times 6]} = (\mathbf{G}_{\tilde{\mathbf{u}}i})_{i \in \mathcal{W}}$  as  $\tilde{\mathbf{u}} = \mathbf{G}_{\tilde{\mathbf{u}}} \mathbf{e}$ , where

$$\mathbf{G}_{\tilde{\mathbf{u}}i} = \frac{1}{2} \begin{bmatrix} 2\tilde{x}_i & 0 & \tilde{y}_i & \tilde{x}_i(h-2z_i) & 0 & \tilde{y}_i(h-2z_i)/2 \\ 0 & 2\tilde{y}_i & \tilde{x}_i & 0 & \tilde{y}_i(h-2z_i) & \tilde{x}_i(h-2z_i)/2 \\ 0 & 0 & 0 & \tilde{x}_i(x_i+x_j) & \tilde{y}_i(y_i+y_j) & x_i y_i - x_j y_j \end{bmatrix}. \quad (30)$$

The next step is to calculate the displacements  $\mathbf{u}_0$  of independent nodes using force periodicity, similar to the procedure used for the zigzag lattice in Section 2.3.

### 3.3. Periodicity of forces

Nodal forces  $\mathbf{f} = (\mathbf{f}_i)_{i \in \mathcal{W}}$  are generated under the influence of a macroscopic field on the origami lattice. When multiple fields are applied,  $\mathbf{f}$  encompasses contributions from each field:  $\mathbf{f} = \mathbf{f}^\epsilon + \mathbf{f}^\kappa$ . These nodal forces are related to the nodal displacements  $\mathbf{u}$  through the stiffness matrix, such that  $\mathbf{f} = \mathbf{K}\mathbf{u}$ .

When using the bar and hinge method, the stiffness matrix  $\mathbf{K}$  for the origami unit cell is determined through standard structural analysis procedures (Schenk and Guest, 2011; Filipov et al., 2017). Given the translational periodicity of the lattice, it can be shown that the nodal forces  $\mathbf{f}$  satisfy  $\mathbf{P}^T \mathbf{f} = \mathbf{0}$ . The presence of these additional constraints allows us to find the nodal displacements of the unit cell as  $\mathbf{u} = \mathbf{G}_u \mathbf{e}$  following the procedure outlined for the zigzag lattice in Section 2.3. The form of  $\mathbf{G}_u$  aligns with that of Eqn. 19b.

### 3.4. Effective continuum model

The elastic energy density  $U$  stored in the origami lattice is

$$U = \frac{1}{ha_x a_y} \left( \frac{1}{2} \mathbf{f}^T \mathbf{u} \right) = \frac{1}{2} \mathbf{e}^T \left( \frac{1}{ha_x a_y} \mathbf{G}_u^T \mathbf{K} \mathbf{G}_u \right) \mathbf{e} \quad (31)$$

where we use  $\mathbf{f} = \mathbf{K} \mathbf{u}$  and  $\mathbf{u} = \mathbf{G}_u \mathbf{e}$ . To find an equivalent continuum for the origami lattice, we compare this expression of elastic density with that of a couple-stress medium subjected to the same macroscopic fields  $\mathbf{e}$ . The elastic energy density  $U_{\text{eff}}$  for a couple-stress effective medium is given as:

$$U_{\text{eff}} = \frac{1}{2} \mathbf{e}^T \mathbf{C} \mathbf{e}. \quad (32)$$

In this equation,  $\mathbf{C}_{[6 \times 6]}$  is the effective elasticity matrix that relates  $\mathbf{e}_{[6 \times 1]}$  (comprising strains  $\boldsymbol{\epsilon}_{[3 \times 1]}$  and curvatures  $\boldsymbol{\kappa}_{[3 \times 1]}$ ) to the internal stresses  $\boldsymbol{\tau}_{[6 \times 1]}$  (including force-stresses  $\boldsymbol{\sigma}_{[3 \times 1]}$  and couple-stresses  $\boldsymbol{\mu}_{[3 \times 1]}$ ) through the constitutive relation  $\boldsymbol{\tau} = \mathbf{C} \mathbf{e}$ . By equating the expressions for the elastic energy density of the lattice with that of the homogeneous medium, we find  $\mathbf{C}$  as:

$$\mathbf{C} = \frac{1}{ha_x a_y} \mathbf{G}_u^T \mathbf{K} \mathbf{G}_u. \quad (33)$$

This matrix can be divided into three sub-matrices, each of size  $3 \times 3$ :  $\mathbf{A}$ ,  $\mathbf{B}$  and  $\mathbf{D}$ , like shown for the 1D case in Eqn. 21b. Sub-matrix  $\mathbf{A}$  is the Cauchy's elasticity matrix, relating in-plane strains  $\boldsymbol{\epsilon}$  to force-stresses  $\boldsymbol{\sigma}$  (Fig. 9a), while sub-matrix  $\mathbf{D}$  relates curvatures  $\boldsymbol{\kappa}$  to couple-stresses  $\boldsymbol{\mu}$  (Fig. 9b). The off-diagonal component  $\mathbf{B}$  represents the coupling between in-plane and out-of-plane behavior. For centrosymmetric lattices, in-plane forces are related only to in-plane deformations, and net moments are related solely to out-of-plane deformations. Examples of centrosymmetric patterns include Miura-ori (Schenk and Guest, 2013; Wei et al., 2013), Eggbox (Schenk, 2012; Nassar et al., 2017), Morph (Pratapa et al., 2019, 2021) and tri-Morph (Liu et al., 2022). However, origami lattices without centrosymmetry may exhibit coupling between in-plane and out-of-plane fields (discussed later in this paper).

Next, we delve into the physical interpretations of  $\mathbf{C}$  derived from the presented framework.

### 3.5. Effective metamaterial constants

The elasticity matrix components hold physical significance that can be derived from straightforward laboratory tests on the origami metamaterial.

In-plane tests: Uniaxial stress  $\sigma_x$  along the  $x$ -axis causes  $\epsilon_x = \sigma_x/E_x$ , where  $E_x$  is the  $x$ -direction Young's modulus; transverse strain  $\epsilon_y$  is estimated from stretching Poisson's ratio  $\nu_{xy}^s$  as  $\epsilon_y = -\nu_{xy}^s \sigma_x/E_x$ . Similar tests along the  $y$ -direction yield  $\epsilon_y = \sigma_y/E_y$  and  $\epsilon_x = -\nu_{yx}^s \sigma_y/E_y$ , where  $E_y$  is the  $y$ -direction Young's modulus and  $\nu_{yx}^s$  is the stretching Poisson's ratio for uniaxial stress  $\sigma_y$ . In a symmetric shear test,  $\epsilon_{xy} = \epsilon_{yx} = 0.5 \sigma_{xy}/G_{xy}$ , where  $\sigma_{xy}$  is the shear stress, and  $G_{xy}$  is the shear modulus of the metamaterial.

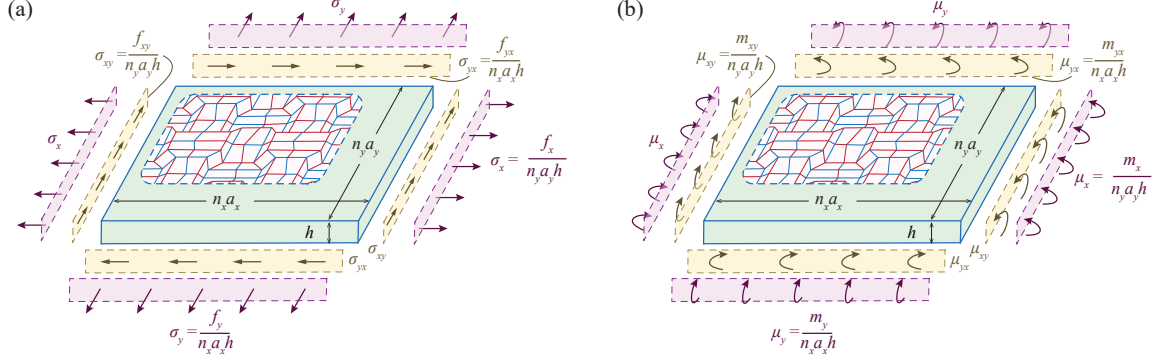


Figure 9: A Kirchhoff-Love plate model for the homogeneous response of planar origami metamaterials subjected to strain and curvature fields. Internal stresses generated within the medium are separated into (a) force-stresses, appearing as distributed forces, and (b) couple-stresses, appearing as distributed moments.

Out-of-plane tests: Uniaxial couple-stress  $\mu_x$  applied along the  $x$ -axis leads to curvatures  $\kappa_x = \mu_x/M_x$  and  $\kappa_y = -\nu_{xy}^b \mu_x/M_x$ , where  $M_x$  represents the  $x$ -axis bending modulus, and  $\nu_{xy}^b$  is the bending Poisson's ratio for  $\mu_x$ . Similar test along the  $y$ -direction result in  $\kappa_y = \mu_y/M_y$  and  $\kappa_x = -\nu_{yx}^b \mu_y/M_y$ , where  $M_y$  is the  $y$ -axis bending modulus, and  $\nu_{yx}^b$  is the bending Poisson's ratio for  $\mu_y$ . In a twisting test,  $\kappa_{xy} = \kappa_{yx} = 0.5\mu_{xy}/T_{xy}$ , where  $\mu_{xy}$  is the twisting couple-stress, and  $T_{xy}$  is the twisting modulus.

Many origami patterns, including the ones like Miura-ori, Eggbox, and Morph, demonstrate a behavior where shear-axial and twisting-bending responses are decoupled (Schenk, 2012; Wei et al., 2013; Pratapa et al., 2019). This decoupling is similar to the behavior observed in orthotropic continuum materials (Reddy, 2013). Furthermore, when origami patterns exhibit centrosymmetry, in-plane and out-of-plane deformations become entirely decoupled. In such scenarios, the relationships presented in the previous discussion can be succinctly represented as

$$\begin{bmatrix} \epsilon_x \\ \epsilon_y \\ 2\epsilon_{xy} \\ \kappa_x \\ \kappa_y \\ 2\kappa_{xy} \end{bmatrix} = \begin{bmatrix} 1/E_x & -\nu_{yx}^s/E_y & 0 & 0 & 0 & 0 \\ -\nu_{xy}^s/E_x & 1/E_y & 0 & 0 & 0 & 0 \\ 0 & 0 & 1/G_{xy} & 0 & 0 & 0 \\ 0 & 0 & 0 & 1/M_x & -\nu_{yx}^b/M_y & 0 \\ 0 & 0 & 0 & -\nu_{xy}^b/M_x & 1/M_y & 0 \\ 0 & 0 & 0 & 0 & 0 & 1/T_{xy} \end{bmatrix} \begin{bmatrix} \sigma_x \\ \sigma_y \\ \sigma_{xy} \\ \mu_x \\ \mu_y \\ \mu_{xy} \end{bmatrix}, \quad (34)$$

The compliance matrix presented in Eqn. 34 is denoted as  $\mathbf{S}_{[6 \times 6]}$  and is the inverse of the elasticity matrix  $\mathbf{C}_{[6 \times 6]}$ . Among the ten metamaterial constants listed above, not all are independent as the following constraints exist for  $\mathbf{S}$  to be symmetric:

$$\nu_{xy}^s E_y = \nu_{yx}^s E_x, \quad (35a)$$

$$\nu_{xy}^b M_y = \nu_{yx}^b M_x. \quad (35b)$$

So far, this section detailed the process of finding an effective continuum that represent the homogenized response of planar origami metamaterials. The following sub-section provides a concise flowchart outlining the essential steps of this homogenization framework for convenient reference.

### 3.6. Steps for homogenization of planar origami metamaterials

The critical steps of the proposed framework for homogenizing planar origami metamaterials into a couple-stress continuum, resembling a Kirchhoff-Love plate model, are condensed into a

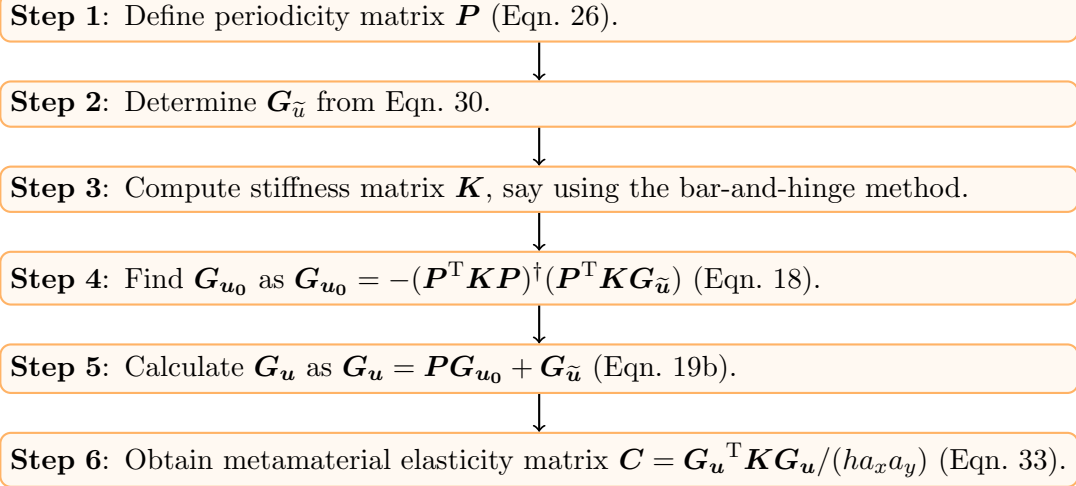


Figure 10: Steps to homogenize planar origami metamaterial as a couple stress continuum.

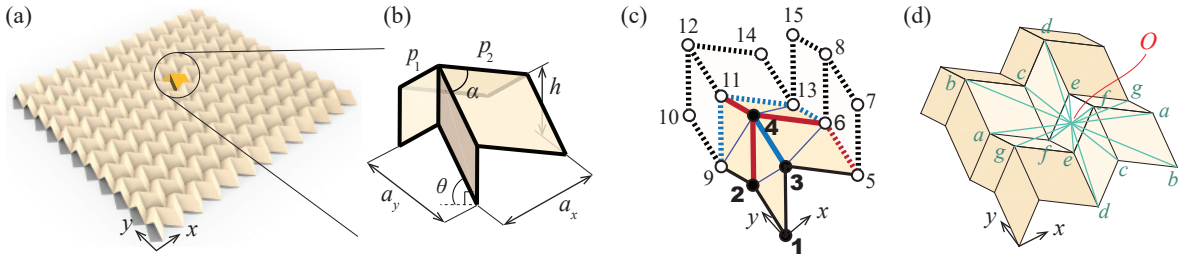


Figure 11: (a) A finite tessellation of the Miura-ori lattice. (b) Unit cell dimensions. (c) Bar-and-hinge model of the unit cell. (d) The lattice is centrosymmetric about point  $O$ .

flowchart and illustrated in Fig. 10. The critical steps of the proposed framework for homogenizing planar origami metamaterials into a couple-stress continuum, resembling a Kirchhoff-Love plate model, are condensed into a flowchart and illustrated in Fig. 10. We have applied this framework to homogenize well known origami patterns including Miura-ori, Eggbox, and Morph. For brevity, the following section focus on discussing the results specifically related to the well-known Miura-ori pattern.

#### 4. Homogenization of Miura-ori

This section demonstrates the application of the proposed framework on the Miura-ori pattern (Fig. 11a, b). Figure 11c shows the bar-and-hinge description, where the panels are triangulated by providing bars along the shorter diagonals, in addition to crease locations. Solid and dashed lines in Fig. 11c denote bars of finite and zero axial stiffness, respectively. Besides, red (or blue) color indicates a finite rotational hinge stiffness about the bar to account for mountain (or valley) crease folding. Further, thin violet lines indicate a finite rotational hinge stiffness about the bar to account for panel bending. No rotational hinges are considered about the black bars.

We begin by establishing the periodicity relation  $\mathbf{P}$  for the lattice. The unit cell has a total of  $n = 15$  nodes, among which  $n_0 = 4$  are independent; the positions of other nodes are dependent on these. From geometric periodicity, we find  $\mathbf{P} = \{(1, 1), (2, 2), (3, 3), (4, 4), (5, 1), (6, 2), (7, 3), (8, 4), (9, 1), (10, 2), (11, 3), (12, 4), (13, 1), (14, 2), (15, 3)\}$ . To find the matrix  $\mathbf{G}_{\tilde{u}}$  (from Eqn. 30), we determine the unit cell dimensions from geometry (Schenk and Guest, 2013), considering that

Table 2: Geometric and stiffness parameters chosen for modeling the Miura-ori cell

$p_2(\text{mm})/p_1(\text{mm})$	$\alpha(\text{deg})$	$\theta(\text{deg})$	$k_b(\text{Nmm})/k_f(\text{Nmm})$	$k_a(\text{N})p_1(\text{mm})/k_f(\text{Nmm})$
1	$60^\circ$	$45^\circ$	10	$10^{10}$

the parallelogram panels have edge lengths  $p_1$  and  $p_2$  and angle  $\alpha$ . The dimensions are:

$$a_x = 2p_2 \cos \theta \tan \alpha (1 + \cos^2 \theta \tan^2 \alpha)^{-1/2}, \quad (36a)$$

$$a_y = 2p_1 (1 - \sin^2 \alpha \sin^2 \theta)^{1/2}, \quad (36b)$$

$$h = p_1 \sin \theta \sin \alpha. \quad (36c)$$

We calculate the stiffness matrix  $\mathbf{K}_{[45 \times 45]}$  for the unit cell considering compatibility, constitutive relations, and equilibrium equations. Following which we determine the linear function  $\mathbf{G}_{\mathbf{u}\mathbf{0}}_{[12 \times 6]}$  (from Eqn. 18) and  $\mathbf{G}_{\mathbf{u}}_{[45 \times 6]}$  (from Eqn. 19b) to connect the displacement of the unit cell to macroscopic fields. Finally, we estimate the elasticity matrix  $\mathbf{C}_{[6 \times 6]}$  for the effective medium using Eqn. 33. In the next section, we discuss the results for specific unit cell dimensions.

#### 4.1. Results and discussion

Typical numerical values are considered to model the Miura-ori cell:  $p_2/p_1 = 1$ ,  $\alpha = 60^\circ$ ,  $k_a = 10^{10}k_f/p_1$ , and  $k_b/k_f = 10$ . Here,  $k_f$  and  $k_b$  are the stiffness against crease folding and panel bending respectively, and  $k_a$  is the axial rigidity of the bars. These numerical values aim to make the system behavior closely resemble that of rigid origami with triangulated panels, allowing for comparison with prior studies. Initially, we perform the homogenization at a single folded state at  $\theta = 45^\circ$ . Later, a parametric study with  $\alpha$  and  $\theta$  will be presented. The normalized numerical values for the parameters are listed in Table 2 for quick reference. Following the steps in Fig. 10, we find the metamaterial elasticity matrix  $\mathbf{C}$  (to two decimal points) to be

$$\mathbf{C} = \frac{10^9 k_f}{p_1^3} \begin{bmatrix} 7.27 & -4.85 & 0.00 & 0.00p_1 & 0.00p_1 & 0.00p_1 \\ -4.85 & 3.23 & 0.00 & 0.00p_1 & 0.00p_1 & 0.00p_1 \\ 0.00 & 0.00 & 5.00 & 0.00p_1 & 0.00p_1 & 0.00p_1 \\ 0.00p_1 & 0.00p_1 & 0.00p_1 & 0.55p_1^2 & 0.37p_1^2 & 0.00p_1^2 \\ 0.00p_1 & 0.00p_1 & 0.00p_1 & 0.37p_1^2 & 0.24p_1^2 & 0.00p_1^2 \\ 0.00p_1 & 0.00p_1 & 0.00p_1 & 0.00p_1^2 & 0.00p_1^2 & 0.00p_1^2 \end{bmatrix}. \quad (37)$$

The absence of off-diagonal coupling terms ( $\mathbf{B} = 0$ ) in the  $\mathbf{C}$  is a consequence of centrosymmetry in the lattice, while the decoupling of shear (and twisting) deformations from axial (and bending) deformations is evident through the components  $C_{13}$ ,  $C_{23}$ ,  $C_{46}$ , and  $C_{56}$  all being zero. These observations align with that made in the study of rigid origami structures (Schenk, 2012; Wei et al., 2013). When examining the units of the elasticity matrix components, the sub-matrix  $\mathbf{A}$  has units of stress ( $\text{N}/\text{mm}^2$ ), which can also be expressed as units of  $k_f/p_1^3$  ( $\text{Nmm}/\text{mm}^3$ ), as it relates strains (no units) to force-stresses ( $\text{N}/\text{mm}^2$ ). On the other hand, sub-matrix  $\mathbf{D}$  has units of force (N) or units of  $k_f/p_1$  ( $\text{Nmm}/\text{mm}$ ), effectively transforming curvatures ( $1/\text{mm}$ ) into couple-stresses ( $\text{N}/\text{mm}$ ). The coupling term  $\mathbf{B}$  is measured in units of ( $\text{N}/\text{mm}$ ), connecting either curvatures ( $1/\text{mm}$ ) to force-stresses ( $\text{N}/\text{mm}^2$ ) or strains (no units) to couple-stresses ( $\text{N}/\text{mm}$ ).

The effective metamaterial constants, calculated using Eqn. 34, are presented in a normalized form in Table 3. Their physical interpretations for tessellations made from real materials are provided in Section S4 of the supplementary material. These constants remain consistent irrespective of the number of cells, given it is sufficiently large, as they are representative of the homogeneous

Table 3: Normalized effective metamaterial constants of Miura-ori with parameters given in Table 2:  $p_2/p_1 = 1$ ,  $\alpha = 60^\circ$ ,  $\theta = 45^\circ$ ,  $k_b/k_f = 10$ ,  $k_a p_1/k_f = 10^{10}$

$E_x p_1^3/k_f$	$E_y p_1^3/k_f$	$G_{xy} p_1^3/k_f$	$M_x p_1/k_f$	$M_y p_1/k_f$	$T_{xy} p_1/k_f$	$\nu_{xy}^s$	$\nu_{yx}^s$	$\nu_{xy}^b$	$\nu_{yx}^b$
109.33	48.59	$5.00 \times 10^9$	44.25	19.67	7.33	-1.50	-0.67	1.50	0.67

response of the lattice. However, scaling up (or down) the unit cell results in the effective stiffness parameters decreasing (or increasing), as all the moduli are inversely related to the panel length  $p_1$  raised to a positive integer (Table 3). This intriguing observation is contrary to the common intuition that homogenized properties should not depend on the scale of the microstructure. Such an understanding comes from the behavior of lattices that can fit into Cauchy continuum model. Nevertheless, origami metamaterials fall outside Cauchy regime and need independent curvature fields for their complete characterization. Because of these separated in-plane and out-of-plane fields, they show different scaling law in the corresponding responses; while the in-plane moduli are proportional to  $k_f/p_1^3$ , out-of-plane moduli scale as  $k_f/p_1$ . It is noteworthy that couple-stress models are in general scale-dependent Hadjesfandiari and Dargush (2011). Moreover, if the folding stiffness  $k_f$  is taken to vary with  $p_1^3$  (as shown in Filipov et al. (2017)), then in-plane responses become scale-independent (like traditional lattices following Cauchy’s theory), while out-of-plane responses scale as  $p_1^2$ . This quadric scaling of out-of-plane responses is consistent with findings on other couple-stress materials Park and Gao (2006).

Furthermore, we observe that the shear modulus  $G_{xy} = 5 \times 10^9 k_f/p_1^3$  in Table 3 is exceptionally high, comparable to the axial rigidity  $k_a = 10^{10} k_f/p_1$  of the bars. This indicates a significant contribution from bar extension under shear stresses, implying that a Miura-ori lattice with idealized rigid triangulated panels would exhibit no deformation under pure shear loading. Nevertheless, bar stretching plays a negligible role in other tests, as reflected in the low values of other moduli. These observations aligns with that from prior studies on rigid Miura-ori systems.

Regarding Poisson’s ratios in Table 3, it is noteworthy that values corresponding to stretching tests are negative ( $\nu_{xy}^s = -1.5, \nu_{yx}^s = -0.67$ ) and are equal and opposite to those obtained from bending tests ( $\nu_{xy}^b = 1.5, \nu_{yx}^b = 0.67$ ), in their respective directions. This behavior deviates from conventional materials but is effectively captured by the present homogenization framework. Moreover, the Poisson’s ratio in perpendicular directions exhibits an inverse relationship. For example,  $\nu_{xy}^s = -3/2 = 1/\nu_{yx}^s$ . This result arises due to the near-single-*dof* behavior of the lattice under axial strain and bending fields, attributed to the bars’ high resistance to elongation. Here, we remark that these Poisson values match exactly with the analytical results reported in previous studies on rigid systems (Schenk, 2012). One consequence of the inverse relation between Poisson’s ratios in perpendicular directions is that the pattern yields a higher Young’s modulus  $E$  in the  $x$ - direction compared to the  $y$ - direction (at  $\theta = 45^\circ$ , refer Table 3). This is explained by  $E_x/E_y = \nu_{xy}^s/\nu_{yx}^s = 2.25$ , taken from Eqn. 35. A similar rationale applies for the relation between the bending moduli in  $x$ - and  $y$ - directions.

In the subsequent study, we explore how the folded state  $\theta$  affect the mechanical properties of the Miura-ori pattern. The variations in the properties with the folded state of origami are referred to as tuneability plots, as they demonstrate the ability of the system to undergo a seamless change in geometry to tune the values of a physical property of interest. We present these plots for different panel angles:  $\alpha = 30^\circ, 45^\circ, 60^\circ$  and  $75^\circ$  in Fig. 12. It is apparent from the figure that the Poisson’s ratio values obtained from this study closely match the analytical predictions for the entire range of folded states and for all considered panel angles.

Of other elastic constants, we first discuss the results pertaining to in-plane constants, followed

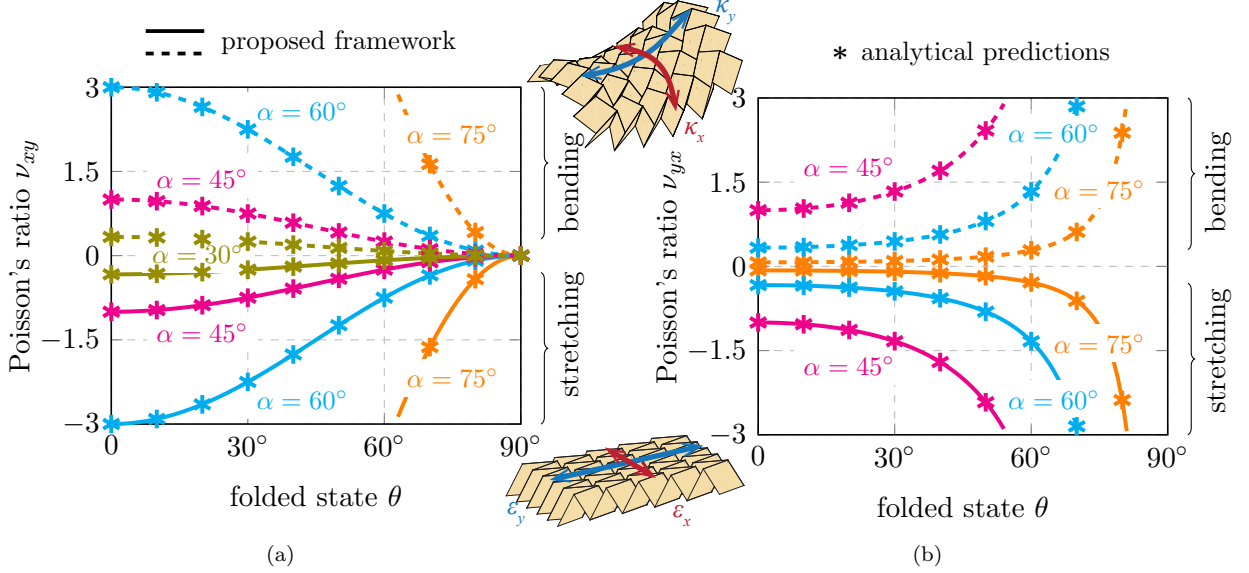


Figure 12: Tuneability plots of Poisson's ratio for various panel angles obtained from the proposed framework (indicated by lines) matches closely with the results from analytical expressions (indicated by asterisk markers). The uniaxial stresses are applied along  $x$ -axis and  $y$ -axis in (a) and (b), respectively. In both plots, positive and negative values correspond to bending (dashed lines) and while stretching test (solid lines), respectively.

by a discussion on out-of-plane constants. The plots for in-plane elastic constants for different panel angles  $\alpha$  are shown in Fig. 13. Starting from the deployed state, we observe that both  $E_x$  and  $G_{xy}$  decrease monotonically (Figs. 13a, c) as the lattice folds with increasing  $\theta$ , indicating that it gets progressively easier to open up the rotational hinges as lattice approaches the folded state. Moreover, in the limit of the fully developed state ( $\theta = 0$ ), the lattice's in-plane stiffness directly relates to the axial stiffness of the panels, which is very high. A similar reason accounts for the higher values of  $E_y$  observed near the developed state (Fig. 13b). But unlike the trend of  $E_x$ , the stiffness along  $y$ -direction increases after reaching a minimum. This is because the panels get aligned along the  $y$ -axis as the lattice folds, making it highly stiff at the limit of fully folded state. Furthermore, the plots show that increasing  $\alpha$  generally increases  $E_x$  values, while reducing  $E_y$  values (Figs. 13a, b). This trend can be understood by noting the variation of  $\nu_{xy}^s$  and  $\nu_{yx}^s$  (in Fig.12) together with the relationship  $E_x/E_y = \nu_{xy}^s/\nu_{yx}^s$  (Eqn. 35).

Tuneability plots for out-of-plane elasticity constants are shown in in Fig. 14 for different panel angles  $\alpha$ . The variation of  $M_x$  (Fig. 14a) is intriguing. The lattice is actually most resistant to  $x$ -direction bending in the deployed state, and it becomes progressively flexible as it approaches the fully folded state. This counter-intuitive behavior parallels that observed in the 1D zigzag lattice (illustrated in Fig. 5), for which a rationale was provided in Section 2.4. The bending stiffness  $M_y$  shown in Fig. 14b exhibits a different trend. It reaches the lowest at an intermediate value of  $\theta$  from which it gets higher at any other state. These trends of  $M_x$  and  $M_y$  (Figs. 14a, b) closely mirror those of  $E_x$  and  $E_y$  (Figs. 13a, b) due to the relationship  $M_x/M_y = E_x/E_y$  (as deduced from Eqn.35 and the fact that  $\nu^s = -\nu^b$ ). Interestingly, the twisting modulus  $T_{xy}$  presented in Fig. 14c attains minimum at  $\theta = 45^\circ$  irrespective of panel angle  $\alpha$ , and gets stiffer by an exact same amount when folded or unfolded by equal amount from that state.

#### 4.2. Numerical simulation

To validate the effective material properties derived in this study, we perform numerical simulations on a finite Miura-ori lattice, employing both the bar-and-hinge model and the finite element

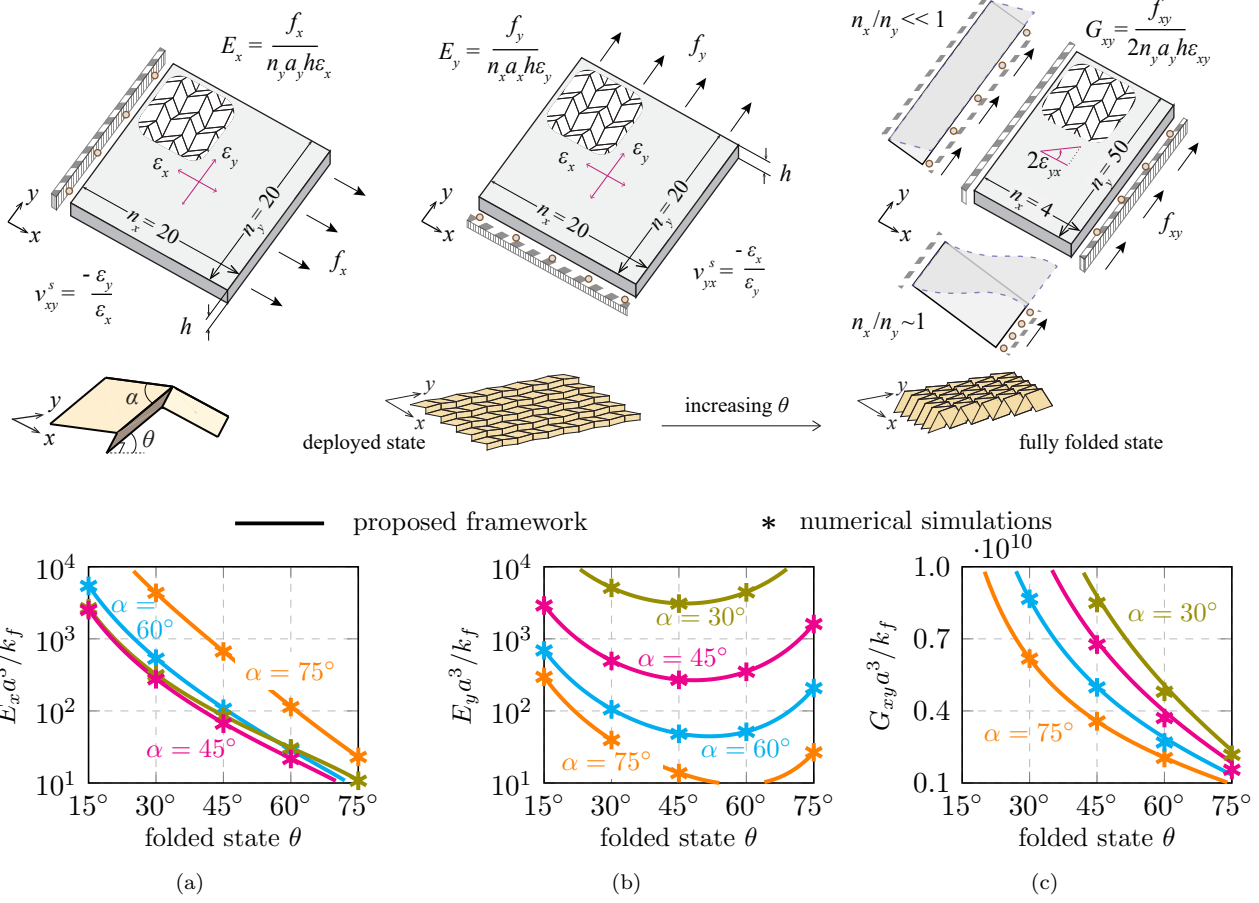


Figure 13: Tuneability plots for in-plane elastic constants of Miura-ori. The top row depicts the loading and boundary conditions on a finite Miura-ori lattice used for numerical simulations (discussed in Section 4.2). The bottom row shows the tuneability plots for in-plane constants (for different panel angles  $\alpha$ ) obtained from the proposed framework. Test details and results corresponding to (a) uniaxial extension along  $x$ , (b) uniaxial extension along  $y$ , and (c) shear test in the  $xy$ -plane.

method. In this subsection, we outline the specifics of the bar-and-hinge model, while the details of the finite element analysis are presented in Section S3 of the supplementary material. The validation comprises six tests, three assessing in-plane behavior and three examining out-of-plane behavior. From a convergence study we find that  $20 \times 20$  cells could sufficiently approximate the homogeneous response of the lattice (except under in-plane shear, where different number of cells are taken). The simulations are repeated at various folded states  $\theta$  and for different panel angles  $\alpha$ . In these simulations, strains or curvatures are calculated using the finite difference technique, while force (or couple) stresses are estimated as area-distributed forces (or moments).

The in-plane behavior is studied through three tests: (a) uniaxial pull along the  $x$ -axis, (b) uniaxial pull along the  $y$ -axis, and (c) shear in the  $xy$ -plane. From the extension simulations, Young's moduli  $E_x$  and  $E_y$  are estimated from axial strains and stresses recorded at the location of an internal cell. Poisson's ratios  $\nu_{xy}^s$  and  $\nu_{yx}^s$  are evaluated by measuring lateral strains. In the shear test, a lattice with  $4 \times 50$  cells is chosen to encourage the extremely stiff shear mode, instead of a more flexible (non-homogeneous) in-plane bending mode (see top row of Fig. 13c). The shear modulus is estimated as the ratio of applied shear stress to induced shear strains.

To characterize the out-of-plane behavior, we conduct three more tests: (a) uniaxial bending

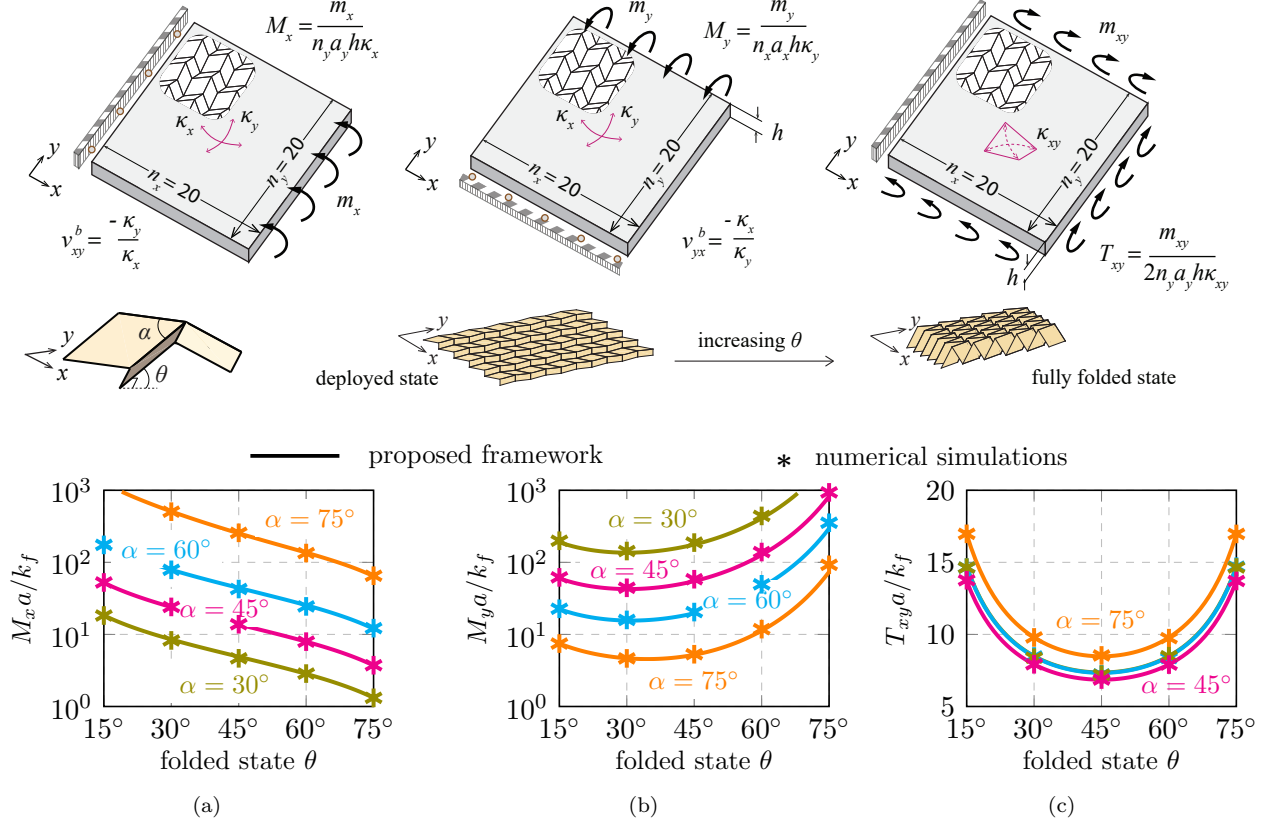


Figure 14: Tuneability plots for normalized out-of-plane elastic constants of Miura-ori. The top row depicts the loading and boundary conditions on a finite Miura-ori lattice used for numerical simulations (discussed in Section 4.2). The bottom row shows the tuneability plots for out-of-plane constants (for different panel angles  $\alpha$ ) obtained from the proposed framework. Test details and results corresponding to (a) uniaxial bending along  $x$ , (b) uniaxial bending along  $y$ , and (c) twisting test in the  $xy$ -plane.

along the  $x$ -direction, (b) uniaxial bending along the  $y$ -direction, and (c) twisting in the  $xy$ -plane. Through the first two tests, bending moduli are estimated from longitudinal curvatures recorded at the location of internal cells for the applied couple-stresses. Bending Poisson's ratios  $\nu_{xy}^b$  and  $\nu_{yx}^b$  are evaluated using transverse curvatures. The twisting modulus is estimated as the ratio of applied couple-stress to induced twisting curvature.

The effective material properties obtained from the simulations are indicated with asterisk (\*) markers in Figs. 13, 14. We observe that, for both in-plane and out-of-plane cases, the homogenized behavior (marked in solid lines) closely matches the results from numerical simulations on finite lattices, validating the proposed framework.

Next, we characterize the elasticity matrix  $\mathbf{C}_{[6 \times 6]}$  by conducting an eigenanalysis. We find the set of six eigenmodes  $\Phi = (\Phi_k)_{k \in [1,6]}$  of the lattice and the corresponding eigenvalues  $\lambda = (\lambda_k)_{k \in [1,6]}$ , that provides information on the energy required for each mode, by solving  $\mathbf{C}\Phi =$

$\text{diag}(\boldsymbol{\lambda})\boldsymbol{\Phi}$ :

$$\boldsymbol{\lambda} = \left[ \begin{array}{cccccc} 7.33 & 13.62 & 33.64/p_1^2 & 10^9 & 10^{10}/p_1^2 & 10^{10}/p_1^2 \end{array} \right] k_f/p_1,$$

$$\boldsymbol{\Phi} = \begin{bmatrix} 0.00 & 0.00 & 0.55 & 0.00 & 0.00 & -0.83 \\ 0.00 & 0.00 & 0.83 & 0.00 & 0.00 & 0.55 \\ 0.00 & 0.00 & 0.00 & 0.00 & 1.00 & 0.00 \\ 0.00 & 0.55 & 0.00 & 0.83 & 0.00 & 0.00 \\ 0.00 & -0.83 & 0.00 & 0.55 & 0.00 & 0.00 \\ 1.00 & 0.00 & 0.00 & 0.00 & 0.00 & 0.00 \end{bmatrix}. \quad (38)$$

We note that the set of eigenmodes  $\boldsymbol{\Phi}$  (in Eqn. 38) are independent of uniform scaling in both structural stiffness (governed by  $k_f$ ) and in unit cell dimension (governed by  $p_1$ ). Nevertheless, eigenvalues depend on both these parameters. Eigenvalues for out-of-plane modes ( $\lambda_1, \lambda_2, \lambda_4$ ) vary inversely with  $p_1$ , while the eigenvalues for in-plane modes ( $\lambda_3, \lambda_5, \lambda_6$ ) vary inversely with  $p_1^3$ . Figure 15 shows the eigenmodes along with the proportion of energy contribution from crease folding, panel bending and panel stretching. Among the six modes, first three modes deform only through crease folding or panel bending, requiring less energy, evident from their eigenvalues  $\lambda_1 = 7.33k_f/p_1$ ,  $\lambda_2 = 13.62k_f/p_1$  and  $\lambda_3 = 33.64k_f/p_1^3$  (Eqn. 38). Twisting mode requires the least energy (Fig. 15a), followed by saddle bending (Fig. 15b). Both these deformation modes are predominantly governed by panel bending ( $\sim 94\%$  energy contribution) and a small extent from crease folding. The third mode is the origami folding mode that is almost entirely dominated by crease folding (Fig. 15c). It is interesting that the first two modes, which are primarily governed by panel bending, exhibit lower energy requirements compared to the third mode, which is dominated by crease folding, even though  $k_b = 10k_f$ . Nevertheless, we remark that this observation corresponds to a specific state of  $\theta = 45^\circ$  and  $p_1 = 1$ . The order gets reversed, with folding mode needing lower energy, for higher values of  $p_1$  and  $\theta$  (near the fully folded state).

The first three modes of the lattice described above have insignificant energy contributions from panel elongation. So, these modes are observed in rigid triangulated Miura-ori systems as zero energy, floppy modes (Schenk and Guest, 2013). The rest of the modes are attained only when panel stretching is allowed, in non-rigid origami structures, requiring high energy for the process (reflected through high  $\lambda$  values in Eqn. 38). These modes correspond to dome bending (Fig. 15d), shearing (Fig. 15e), and in-plane lattice stretching as shown in Fig. 15f.

## 5. Discussion on Non-Centrosymmetric Planar Origami Metamaterials

In origami patterns like Miura-ori, Eggbox, and Morph (Schenk and Guest, 2011; Wei et al., 2013; Pratapa et al., 2019), force-stresses induce only in-plane deformations, while couple-stresses lead to only out-of-plane deformations. These deformations remain uncoupled due to the lattice's centrosymmetry (Fig. 11d). In such cases, the mid-plane also is the neutral surface, where no axial deformations occur due to couple-stresses.

In lattices without centrosymmetry, in-plane and out-of-plane responses can be coupled. In this section, we apply the homogenization framework to one such non-centrosymmetric origami lattice, discussing intriguing findings. Specifically, the chosen non-centrosymmetric origami lattice lacks a unique neutral surface. Instead, the neutral planes under couple-stresses  $\mu_x$  and  $\mu_y$  are distinct, positioned symmetrically on either side of the mid-plane.

### 5.1. Homogenization of non-centrosymmetric lattice

We reconsider the Miura-ori pattern, but this time we remove one-half of a panel from the unit cell, as in kirigami systems (see Fig. 16a). The resulting Miura-ori lattice is no longer centrosym-

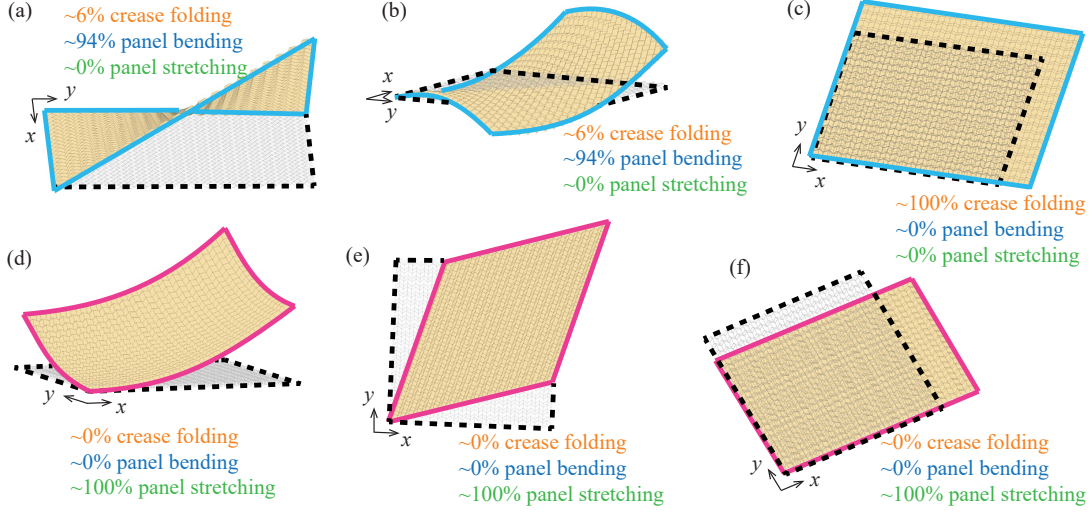


Figure 15: Six eigenmodes of an infinite non-rigid Miura-ori lattice modeled as a couple-stress continuum. The first three modes require low energy: (a) twisting, (b) saddle bending, and (c) origami folding. The other three modes involve panel elongation: (d) dome bending, (e) shearing, and (f) in-plane lattice stretching

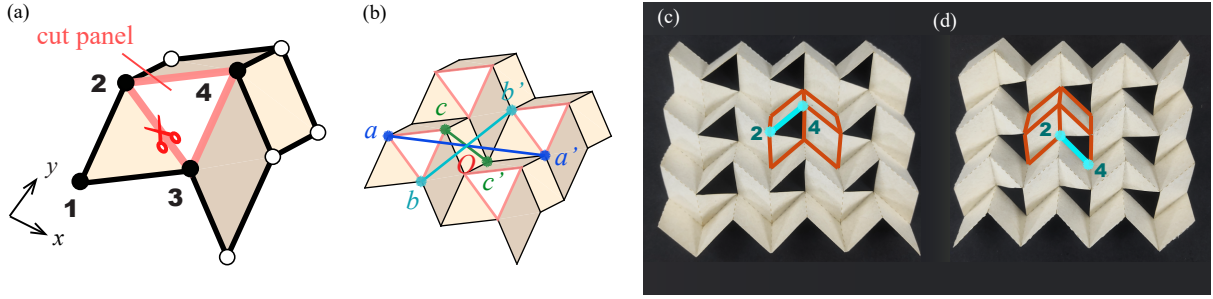


Figure 16: (a) A triangular panel (2 – 3 – 4) is removed from the Miura-ori unit cell. The lattice loses the centrosymmetry due to this cut operation. (b) While triangle  $a'b'c'$  is an inversion of triangle  $abc$  about point  $O$ , the former is a solid uncut panel, whereas the latter is a void region. (c) A  $3 \times 3$  prototype of the modified pattern. (d) When the prototype is inverted, the resulting configuration is not identical to that in (c), illustrating that the lattice is non-centrosymmetric.

metric (as illustrated in Fig. 16b, c, d), as all the cut panels have two vertices on the top (e.g., vertices 2 and 4) but only one on the bottom (e.g., vertex 3). In the context of the bar-and-hinge model, the removal of the panel corresponds to setting the rotational stiffness  $k_b$  about bar 2 – 3, and  $k_f$  about bars 3 – 4 and 2 – 4 to zero, and halving the axial rigidity  $k_a$  of bars 2 – 3, 3 – 4 and 2 – 4. With this change, we homogenize the modified lattice (with parameter values as given in Table 2:  $p_2/p_1 = 1$ ,  $\alpha = 60^\circ$ ,  $k_b/k_f = 10$ ,  $k_a p_1/k_f = 10^{10}$ ) using the same procedure. The effective elasticity matrix  $\mathbf{C}^{nc}$  obtained for the folded state at  $\theta = 45^\circ$  is as follows (rounded to two decimal points):

$$\mathbf{C}^{nc} = \frac{10^9 k_f}{p_1^3} \begin{bmatrix} 5.94 & -3.96 & 0.43 & 0.20p_1 & 0.13p_1 & 0.00p_1 \\ -3.96 & 2.64 & -0.29 & -0.13p_1 & -0.09p_1 & 0.00p_1 \\ 0.43 & -0.29 & 4.08 & 0.16p_1 & 0.11p_1 & 0.00p_1 \\ 0.20p_1 & -0.13p_1 & 0.16p_1 & 0.45p_1^2 & 0.30p_1^2 & 0.00p_1^2 \\ 0.13p_1 & -0.09p_1 & 0.11p_1 & 0.30p_1^2 & 0.20p_1^2 & 0.00p_1^2 \\ 0.00p_1 & 0.00p_1 & 0.00p_1 & 0.00p_1^2 & 0.00p_1^2 & 0.00p_1^2 \end{bmatrix}, \quad (39)$$

Table 4: Normalized effective metamaterial constants of Miura-ori with parameters given in Table 2:  $p_2/p_1 = 1$ ,  $\alpha = 60^\circ$ ,  $\theta = 45^\circ$ ,  $k_b/k_f = 10$ ,  $k_a p_1/k_f = 10^{10}$

Homogenized values from the proposed framework									
$E_x^{nc} p_1^3/k_f$	$E_y^{nc} p_1^3/k_f$	$G_{xy}^{nc} p_1^3/k_f$	$M_x^{nc} p_1/k_f$	$M_y^{nc} p_1/k_f$	$T_{xy}^{nc} p_1/k_f$	$\nu_{xy}^{s,nc}$	$\nu_{yx}^{s,nc}$	$\nu_{xy}^{b,nc}$	$\nu_{yx}^{b,nc}$
81.18	36.08	$4.00 \times 10^9$	30.19	13.42	5.00	-1.50	-0.67	1.50	0.67
Values from numerical simulation on a finite lattice									
80.90	35.85	$4.00 \times 10^9$	31.23	13.20	5.12	-1.50	-0.67	1.50	0.67

The superscript ‘ $nc$ ’ indicates that the results correspond to the non-centrosymmetric lattice. Unlike what was observed for the centrosymmetric case, the off-diagonal term  $\mathbf{B}_{[3 \times 3]}^{nc} \neq \mathbf{O}$ . Therefore, a pure in-plane macroscopic field, such as  $\epsilon_x$ , also generates out-of-plane couple-stresses, such as  $\mu_y$ . Furthermore, we observe that within the in-plane response, axial and shear components are coupled (evident by the non-zero values for  $C_{13}^{nc}$  and  $C_{23}^{nc}$ ). This behavior also differs from that of the original Miura-ori lattice. We next find the elastic constants of the modified Miura-ori lattice and list their normalized forms in Table 4. Their physical interpretations for tessellations made from real materials are provided in Section S4 of the supplementary material. Although more elastic constants are required to characterize this modified lattice, we present only those that essentially hold the same physical meaning as described for the original Miura-ori pattern.

We observe that the values of all moduli (Table 4) are lesser compared to that of the original Miura-ori lattice (Table 3) owing to the panel removal. Yet, the value of Poisson’s ratios remains unchanged because these kinematic quantities are governed only by geometry, and not the stiffness parameters. The shear modulus  $G_{xy}^{nc}$  of the modified lattice is extremely large, while other moduli take much lower values, akin to the observation made on the original Miura-ori lattice.

The set of eigenmodes  $\Phi^{nc} = (\Phi_k^{nc})_{k=[1,6]}$  and the eigenvalues  $\lambda^{nc} = (\lambda_k^{nc})_{k=[1,6]}$  are found as

$$\lambda^{nc} = \begin{bmatrix} 4.62 & 10.91 & 25.41 & 10^9 & 10^9 & 10^{10} \end{bmatrix} k_f, \quad (40)$$

$$\Phi^{nc} = \begin{bmatrix} -0.01 & -0.06 & 0.55 & -0.03 & -0.10 & 0.83 \\ -0.02 & -0.09 & 0.83 & 0.02 & 0.06 & -0.55 \\ 0.00 & 0.00 & 0.00 & -0.05 & 0.99 & 0.11 \\ -0.20 & 0.51 & 0.05 & 0.83 & 0.04 & 0.03 \\ 0.30 & -0.77 & -0.08 & 0.55 & 0.03 & 0.02 \\ 0.93 & 0.36 & 0.06 & 0.00 & 0.00 & 0.00 \end{bmatrix}.$$

For the modified lattice, the eigenvalues and eigenmodes are observed to have a non-trivial dependence on the unit cell scale. In this demonstration, we have set  $p_1 = 1$  to obtain the values in Eqn. 40. The eigenmodes of this lattice are presented in Fig. 17. In contrast to the original Miura-ori lattice, we observe here that the three low-energy modes are not pure bending  $\Phi_1$ , twisting  $\Phi_2$ , or folding  $\Phi_3$  modes given in Eqn. 38. Rather, they are a linear combination of these modes:

$$\Phi_1^{nc} = 1.31(0.71\Phi_1 - 0.27\Phi_2 - 0.01\Phi_3), \quad (41a)$$

$$\Phi_2^{nc} = 1.40(0.26\Phi_1 + 0.66\Phi_2 - 0.08\Phi_3), \quad (41b)$$

$$\Phi_3^{nc} = 1.15(0.05\Phi_1 + 0.08\Phi_2 + 0.87\Phi_3). \quad (41c)$$

The presence of coupling between in-plane and out-of-plane deformations adds complexity and reduces the intuitiveness of the analysis. Such couplings have recently been observed by other

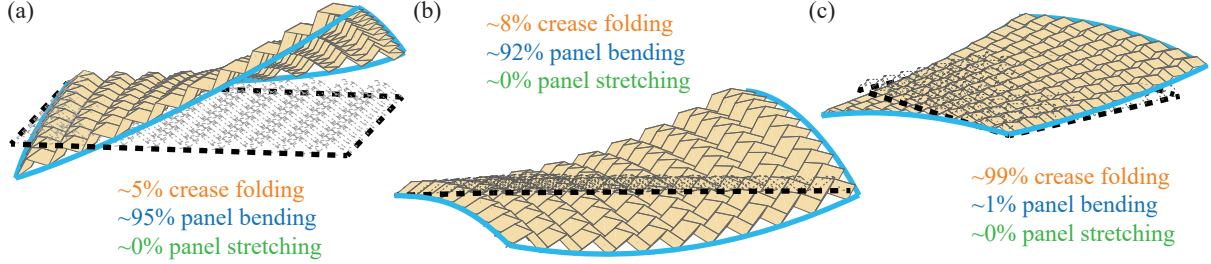


Figure 17: The first three low-energy eigenmodes of non-centrosymmetric Miura-ori lattice. Unlike in the original Miura-ori lattice, these eigenmodes are not pure folding, bending, or twisting, but a linear combination of these three pure modes: (a) Twisting dominant mode, (b) bending dominant mode, and (c) Folding dominant mode.

researchers in a comprehensive study on 3D lattice materials (Cui et al., 2023). In the context of functionally graded plates, where the material is non-uniformly distributed through the thickness, it is known that plates lacking symmetry about the mid-plane can exhibit coupled behavior (Zhang and Zhou, 2008; Thai and Kim, 2015). This coupling in functionally graded plates occurs when the physical neutral surface shifts away from the geometric mid-plane, where in-plane forces are typically considered to act. In such cases, in-plane forces applied at the mid-plane induce moments about the neutral surface, resulting in curvatures of the plate. This insight implies that if the physical neutral surface is treated as the reference, and in-plane forces are applied there, the mentioned coupling can be eliminated, as demonstrated in Abrate (2008).

This discussion begs the question of whether a similar approach can be applied to non-centrosymmetric origami metamaterials. Specifically, can the neutral surface of the origami lattice be chosen as the reference plane<sup>3</sup>, and would this choice eliminate the coupling between in-plane and out-of-plane responses? To address this question, we analyze the locations of the neutral surfaces in the non-centrosymmetric origami metamaterial in the following sub-section. Interestingly, we find that the neutral surfaces for bending along both directions are different. Hence we cannot establish a common neutral surface that could serve as a reference plane for homogenization. So to maintain consistency with the centrosymmetric lattice, we retain the mid-plane as the reference.

## 5.2. Neutral surfaces in non-centrosymmetric lattice

Under the influence of a couple-stress  $\mu_x$ , the lattice undergoes a curvature field  $\kappa_x$ , among other coupled deformation fields. In this configuration, there exists a neutral surface along the lattice height where the relative  $x$  displacements are zero. Let this neutral surface be at  $h_x^*$  (Fig. 18a), which may not coincide with the lattice’s mid-height. Similarly, neutral surfaces for couple-stresses  $\mu_y$  and  $\mu_{xy}$  be at heights  $h_y^*$  and  $h_{xy}^*$ , respectively (Figs. 18b, 18c). We do not depict the coupled fields in Fig. 18 for the sake of simplicity.

To locate of these neutral surfaces, we subject the lattice to three independent stress-controlled uniaxial tests, corresponding to  $\mu_x$ ,  $\mu_y$ , and  $\mu_{xy}$ . In each test, we calculate the deformation field  $\mathbf{e}$  in the lattice from the compliance matrix  $\mathbf{S}^{nc}$ . Then we determine the height along the lattice where the axial (or shear) strains are zero for bending (or twisting). For example, when  $\mu_x = 1$  acts,  $\epsilon_x = S_{14}$  and  $\kappa_x = S_{44}$  are the relevant deformation components. All other deformation quantities ( $\epsilon_y$ ,  $2\epsilon_{xy}$ ,  $\kappa_y$ ,  $2\kappa_{xy}$ ) do not contribute to  $x$ -direction strains. So, the  $x$ -direction strain  $\epsilon_x^z$  at any

<sup>3</sup>We refer to the plane at which we apply forces and measure strains as the “reference plane,” which, in this paper, was chosen as the mid-plane for both the centrosymmetric and non-centrosymmetric lattices. In the centrosymmetric lattice, the mid-plane also coincides with the neutral surface.

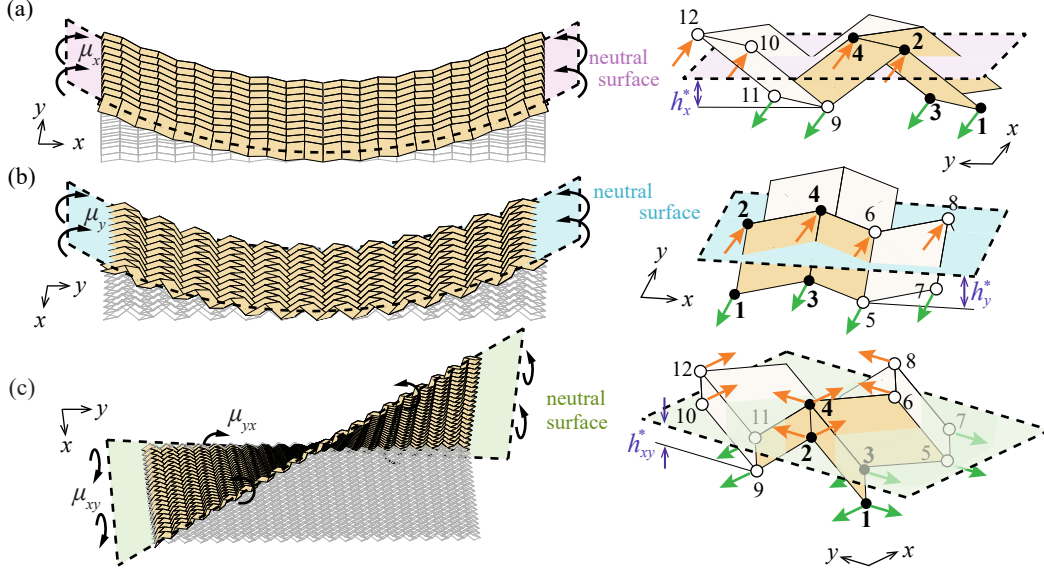


Figure 18: Neutral surfaces for (a) couple-stress  $\mu_x$ , (b) couple-stress  $\mu_y$ , and (c) couple-stress  $\mu_{xy}$ . Neutral surfaces are located along the lattice height where the axial (or shear) strains are zero for stress-controlled bending (or twisting). Although coupled fields could be generated due to the applied stresses, such fields are not shown here for simplicity.

$z$ -level is expressed as:

$$\epsilon_x^z = \epsilon_x + \kappa_x \left( \frac{h}{2} - z \right), \quad (42)$$

At the neutral surface ( $z = h_x^*$ ),  $\epsilon_x^z = 0$ . Therefore, it becomes

$$h_x^* = \frac{h}{2} - \frac{\epsilon_x}{\kappa_x}. \quad (43)$$

Using  $\epsilon_x/\kappa_x = -0.038a$  (from  $\mathbf{S}^{nc}$ ) and  $h/p_1 = 0.61$  (from Eqn. 36) in the above equation, we find  $h_x^*/h = 0.56$ . Similarly, we estimate the values of  $h_y^*$  and  $h_{xy}^*$  for applied  $\mu_y$  and  $\mu_{xy}$ , respectively:

$$h_x^*/h = 0.56, \quad h_y^*/h = 0.44, \quad h_{xy}^*/h = 0.50. \quad (44)$$

We notice that the positions of the neutral surfaces for bending in different directions, as well as for twisting, do not coincide. Therefore, unlike in the centrosymmetric case, here no common neutral surface exists at which all in-plane strains become zero when all three couple-stresses act together. Another interesting observation is that the locations of the neutral surfaces for bending in the  $x$  and  $y$  directions are positioned at equal distances from the mid-plane of the lattice, *i.e.*,  $h_x^* + h_y^* = h$ . This relationship holds true across all folded states  $\theta$  and for different panel angles  $\alpha$ , as demonstrated in Fig. 19. This result directly stems from having equal and opposite Poisson's ratios in stretching and bending, as explained next.

Taking Eqn. 43 as a reference and using a similar equation for the effect of  $\mu_y = 1$ , we find:

$$h_x^* + h_y^* = h - S_{14}M_x - S_{25}M_y. \quad (45)$$

In the above equation, we demonstrate that  $S_{14}M_x + S_{25}M_y = 0$ . For this, firstly note that the modified lattice's deformation occurs primarily within the space spanned by pure folding, bending,

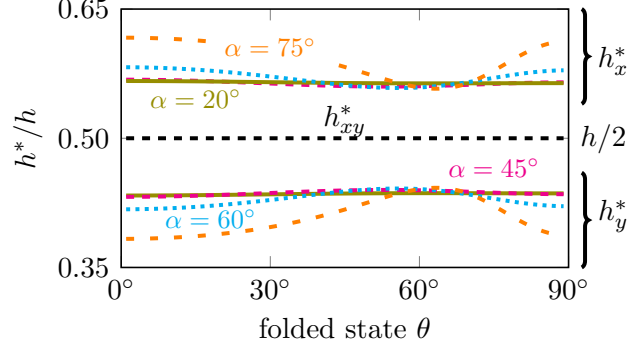


Figure 19: Variation of neutral surface positions  $h_x^*$ ,  $h_y^*$ ,  $h_{xy}^*$  with folded state  $\theta$  for lattices with different panel angles  $\alpha$ . While  $h_{xy}^*$  is at mid-height across the folded states,  $h_x^*$  and  $h_y^*$  vary such that  $h_x^* + h_y^* = h$ .

and twisting modes (Eqn. 41). Consequently, axial strains  $\epsilon_x$  and  $\epsilon_y$  are not independent, rather they are related through the stretching Poisson's ratio  $\nu_{xy}^s$ . Similarly, bending curvatures  $\kappa_x$  and  $\kappa_y$  are related by the bending Poisson's ratio  $\nu_{xy}^b$ . This relationship results in  $S_{24}/S_{14} = \nu_{xy}^s$  and  $S_{25}/S_{15} = \nu_{xy}^s$ . Also, it turns that  $S_{51}/S_{41} = \nu_{xy}^b$  and  $S_{52}/S_{42} = \nu_{xy}^b$ . Multiplying these four expressions together, we find:

$$\frac{S_{25}}{S_{14}} = \nu_{xy}^s \nu_{xy}^b. \quad (46)$$

Using this equation and the relation  $M_x/M_y = (\nu_{xy}^b)^2$  (from Eqn. 35), we deduce:

$$\frac{S_{25}}{S_{14}} + \frac{M_x}{M_y} = \nu_{xy}^b (\nu_{xy}^s + \nu_{xy}^b) = 0, \quad (47)$$

since the Poisson's ratios from stretching and bending are equal and opposite,  $\nu_{xy}^s + \nu_{xy}^b = 0$ . Therefore, Eqn. 45 simplifies to:

$$h_x^* + h_y^* = h. \quad (48)$$

The above result infers that the neutral surfaces for bending in the  $x$ - and  $y$ - directions are distinct and symmetrically situated on either side of the mid-plane, contrasting with conventional materials where they typically coincide.

## 6. Summary and Conclusion

In this study, we presented a framework for evaluating the effective properties of non-rigid planar origami metamaterials homogenized as a couple-stress continuum, akin to a Kirchhoff-Love plate model. This framework utilizes six independent deformation fields consisting of strains and curvatures (strain-gradients), contrasting with typical 2D lattice materials that behave as a Cauchy continuum and require only three strain fields for homogenization. The motivation behind accommodating these extra fields stems from the unique characteristics of origami metamaterials, which exhibit independent in-plane and out-of-plane behavior and feature unconventional relationships between associated Poisson's ratios. These effects are effectively captured through the proposed framework. Furthermore, a mechanics-based definition of origami lattice deformation modes allows for the easy identification of previously unobserved origami modes, such as the twisting of the Morph pattern (Pratapa et al., 2019).

By establishing the elastic constants of the effective continuum, the proposed approach aligns the treatment of origami metamaterials more closely with cellular materials rather than their traditional categorization as mechanism-type systems. Panel stretching was incorporated in the structural analysis through the bar-and-hinge model, allowing for the capture of higher energy modes, such as shear, which are less studied in origami lattices.

The initial application of the homogenization framework focused on centrosymmetric origami lattices like Miura-ori. After validating these results through numerical simulations and analytical predictions, we extended the framework to a non-centrosymmetric lattice, specifically a kirigami-type structure derived from Miura-ori by removing a triangular panel. While the relationship between the bending and stretching Poisson’s ratio remained consistent with the centrosymmetric case, some intriguing features emerged; we identified two distinct neutral surfaces symmetrically positioned to the mid-plane and observed the coupling of in-plane and out-of-plane deformations.

The primary goal of introducing this homogenization framework is to enable the design of architected metamaterials that can replicate the unique property of origami, displaying equal and opposing Poisson’s ratios in stretching and bending. Design of such systems can be realized through inverse homogenization techniques, such as topology optimization. Architecting metamaterials that replicate this property serves at-least two purposes. Firstly, it can provide valuable insights into the underlying mechanisms of the peculiar behavior of origami. Furthermore, these designs could introduce a class of lattice metamaterials with distinct Poisson’s ratios in stretching and bending. Traditional materials exhibit equal Poisson’s ratios in both bending and stretching, while origami structures display opposing values. The question of whether engineered lattices can exhibit any independent Poisson values in bending and stretching remains open. As Poisson’s ratio is a fundamental metric that characterizes the elastic performance of materials, engineering structures with tailored Poisson’s ratios in stretching and bending holds potential for future applications. For example, the effect of in-plane Poisson’s ratio on bending has been used in creating actuators for robots (Hasse and Mauser, 2020). The proposed framework can facilitate the design of such origami-inspired metamaterials, composed of truss, beam, or continuum elements, through inverse-homogenization techniques.

Future research may involve extending the framework for homogenizing origami metamaterials with large displacements, using nonlinear analysis methods (Liu and Paulino, 2017). Additionally, exploring the inclusion of other modes, such as out-of-plane shear, is relevant for specific origami patterns. Furthermore, application of this framework to origami lattices with a broader range of deformations, as studied in Lahiri and Pratapa (2023), presents an interesting direction for future research.

## Acknowledgement

SPV acknowledges the support from the fellowship offered by Prime Minister’s Research Fellows (PMRF) Scheme, Ministry of Human Resource Development, Government of India. PPP acknowledges the support from the Indian Institute of Technology Madras through the seed grant and the Science & Engineering Research Board (SERB) of the Department of Science & Technology, Government of India, through award SRG/2019/000999. The information provided in this paper is the sole opinion of the authors and does not necessarily reflect the views of the sponsors or sponsoring agencies.

## Notation

The following symbols are used in this paper.

$a_x, a_y$	magnitudes of lattice vectors;
$\mathbf{A}$	matrix of elastic constants relating $\boldsymbol{\epsilon}$ to $\boldsymbol{\sigma}$ (size $1 \times 1$ for 1D lattice and $3 \times 3$ for 2D lattice);
$\mathbf{B}$	matrix of elastic constants representing in-plane and out-of-plane coupling (size $1 \times 1$ for 1D lattice and $3 \times 3$ for 2D lattice);
$\mathbf{C}$	elasticity matrix relating $\mathbf{e}$ to $\boldsymbol{\tau}$ (size $2 \times 2$ for 1D lattice and $6 \times 6$ for 2D lattice);
$\mathbf{D}$	matrix of elastic constants relating $\boldsymbol{\kappa}$ to $\boldsymbol{\mu}$ (size $1 \times 1$ for 1D lattice and $3 \times 3$ for 2D lattice);
$\mathbf{e}$	macroscopic deformation field containing $\boldsymbol{\epsilon}$ and $\boldsymbol{\kappa}$ (size $2 \times 1$ for 1D lattice and $6 \times 1$ for 2D lattice);
$\hat{\mathbf{e}}_x, \hat{\mathbf{e}}_y$	unit vectors along $x$ - and $y$ - axes;
$E_x, E_y$	homogenized Young's moduli in $x$ - and $y$ - directions;
$\mathbf{f}$	nodal forces (size $2n \times 1$ for 1D lattice and $3n \times 1$ for 2D lattice);
$G_{xy}$	shear modulus in $xy$ -plane;
$\mathbf{G}_u$	matrix relating $\mathbf{e}$ to $\mathbf{u}$ (size $2n \times 2$ for 1D lattice and $3n \times 6$ for 2D lattice);
$\mathbf{G}_{\tilde{u}}$	matrix relating $\mathbf{e}$ to $\tilde{\mathbf{u}}$ (size $2n \times 2$ for 1D lattice and $3n \times 6$ for 2D lattice);
$\mathbf{G}_{u_0}$	matrix relating $\mathbf{e}$ to $\mathbf{u}_0$ (size $2n_0 \times 2$ for 1D lattice and $3n_0 \times 6$ for 2D lattice);
$h$	lattice height;
$h_x^*$	neutral surface location for bending along $x$ - direction;
$h_y^*$	neutral surface location for bending along $y$ - direction;
$h_{xy}^*$	neutral surface location for lattice twisting in $xy$ -plane;
$i$	index of a node in set $\mathcal{W}$ ;
$\mathbf{I}$	identity matrix; (size $2 \times 2$ for 1D lattice and $3 \times 3$ for 2D lattice)
$j$	index of a node in set $\mathcal{W}_0$ ;
$k_a$	axial rigidity of bars modeling panel stretching;
$k_b$	rotational stiffness of hinges modeling panel bending;
$k_f$	rotational stiffness of hinges modeling crease folding;
$k_h$	rotational stiffness of hinges in 1D lattice;
$k_s$	axial stiffness of bars in 1D lattice;
$\mathbf{K}$	stiffness matrix relating $\mathbf{u}$ to $\mathbf{f}$ (size $2n \times 2n$ for 1D lattice and $3n \times 3n$ for 2D lattice);
$m_x, m_y$	uniform bending moments in the lattice corresponding to resultants of couple stresses;
$M_x, M_y$	bending moduli in $x$ - and $y$ - directions;
$n$	total number of nodes in the unit cell; size of set $\mathcal{W}$ ;
$n_0$	number of independent nodes in the unit cell; size of set $\mathcal{W}_0$ ;
$\mathbf{O}$	null matrix;
$p_1, p_2$	panel lengths of Miura-ori cell;
$P$	periodicity relation represented as a set of ordered pairs relating every node to a corresponding independent node;

$P$	Boolean matrix of $P$ (size $2n \times 2n_0$ for 1D lattice and $3n \times 3n_0$ for 2D lattice);
$r$	position vector of a node (size $1 \times 1$ for 1D lattice and $2 \times 1$ for 2D lattice);
$s_x, s_y$	any integer;
$T_{xy}$	twisting modulus in $xy$ -plane;
$\mathbf{u}_0$	displacements of independent nodes in the unit cell (size $2n_0 \times 1$ for 1D lattice and $3n_0 \times 1$ for 2D lattice);
$\tilde{\mathbf{u}}$	relative displacements of all nodes in the unit cell (size $2n \times 1$ for 1D lattice and $3n \times 1$ for 2D lattice);
$\mathbf{u}$	displacement of all nodes in the unit cell (size $2n \times 1$ for 1D lattice and $3n \times 1$ for 2D lattice);
$U, U_{\text{eff}}$	elastic energy density in lattice and in effective medium;
$x, y, z$	coordinates of a node;
$\tilde{x}, \tilde{y}, \tilde{z}$	nodal coordinates with reference to respective independent node;
$\alpha$	acute panel angle of Miura-ori cell;
$\epsilon$	macroscopic strain field (size $1 \times 1$ for 1D lattice and $3 \times 1$ for 2D lattice);
$\theta$	angle denoting the folded state of a lattice;
$\kappa$	macroscopic curvature field (size $1 \times 1$ for 1D lattice $3 \times 1$ for 2D lattice);
$\nu^s$	Poisson's ratio under in-plane stretching;
$\nu^b$	Poisson's ratio under out-of-plane bending;
$\nu_{xy}$	Poisson's ratio for uniaxial stress applied along $x$ -axis;
$\nu_{yx}$	Poisson's ratio for uniaxial stress applied along $y$ -axis;
$\lambda$	row vector containing eigenvalues (size $1 \times 6$ for 2D lattice);
$\mu$	couple-stresses represented as a column matrix (size $1 \times 1$ for 1D lattice and $3 \times 1$ for 2D lattice);
$\sigma$	force-stresses represented as a column matrix (size $1 \times 1$ for 1D lattice and $3 \times 1$ for 2D lattice);
$\tau$	stress field represented as a column matrix, containing $\sigma$ and $\mu$ (size $2 \times 1$ for 1D lattice and $6 \times 1$ for 2D lattice);
$\Phi$	matrix containing eigenvectors (size $6 \times 6$ for 2D lattice);
$\omega$	rotations of all the nodes in the unit cell (size $n \times 1$ for 1D lattice and $2n \times 1$ for 2D lattice);
$\tilde{\omega}$	rotation of all the nodes in the unit cell relative to their respective independent nodes (size $n \times 1$ for 1D lattice and $2n \times 1$ for 2D lattice);
$\mathcal{W}$	set of all nodes that capture unit cell deformation (e.g., $\mathcal{W} = \{1, 2, 3, 4\}$ for the 1D lattice);
$\mathcal{W}_0$	set of independent nodes in the unit cell (e.g., $\mathcal{W}_0 = \{1, 2\}$ for the 1D lattice);

## References

- Abdoul-Anziz, H., Seppecher, P., 2018. Strain gradient and generalized continua obtained by homogenizing frame lattices. *Mathematics and Mechanics of Complex Systems* 6, 213–250.
- Abrate, S., 2008. Functionally graded plates behave like homogeneous plates. *Composites Part B: Engineering* 39, 151–158.
- Arabnejad, S., Pasini, D., 2013. Mechanical properties of lattice materials via asymptotic homogenization and comparison with alternative homogenization methods. *International Journal of Mechanical Sciences* 77, 249–262.
- Boatti, E., Vasios, N., Bertoldi, K., 2017. Origami metamaterials for tunable thermal expansion. *Advanced Materials* 29.
- Buannic, N., Cartraud, P., Quesnel, T., 2003. Homogenization of corrugated core sandwich panels. *Composite structures* 59, 299–312.
- Cui, Z., Liang, Z., Ju, J., 2022. A non-centrosymmetric square lattice with an axial–bending coupling. *Materials & Design* 216, 110532.
- Cui, Z., Yuan, Z., Ju, J., 2023. Mechanical couplings of 3D lattice materials discovered by micropolar elasticity and geometric symmetry. *Journal of Applied Mechanics* 90, 041001.
- Evans, A.A., Silverberg, J.L., Santangelo, C.D., 2015. Lattice mechanics of origami tessellations. *Physical Review E* 92, 013205.
- Filipov, E.T., Liu, K., Tachi, T., Schenk, M., Paulino, G.H., 2017. Bar and hinge models for scalable analysis of origami. *International Journal of Solids and Structures* 124, 26–45.
- Hadjefandiari, A.R., Dargush, G.F., 2011. Couple stress theory for solids. *International Journal of Solids and Structures* 48, 2496–2510.
- Hassani, B., Hinton, E., 2012. Homogenization and structural topology optimization: theory, practice and software. Springer Science & Business Media.
- Hasse, A., Mauser, K., 2020. Poisson induced bending actuator for soft robotic systems. *Soft Robotics* 7, 155–167.
- Hutchinson, R.G., Fleck, N.A., 2006. The structural performance of the periodic truss. *Journal of the Mechanics and Physics of Solids* 54, 756–782.
- Khakalo, S., Niiranen, J., 2020. Anisotropic strain gradient thermoelasticity for cellular structures: Plate models, homogenization and isogeometric analysis. *Journal of the Mechanics and Physics of Solids* 134, 103728.
- Lahiri, A., Pratapa, P.P., 2023. Lattice modes of periodic origami tessellations with voids. *Mechanics Research Communications* 132, 104167.
- Lebéé, A., Sab, K., 2012. Homogenization of thick periodic plates: Application of the bending-gradient plate theory to a folded core sandwich panel. *International Journal of Solids and Structures* 49, 2778–2792.

- Liu, K., Paulino, G., 2017. Nonlinear mechanics of non-rigid origami: An efficient computational approach. *Proceedings of the Royal Society A: Mathematical, Physical and Engineering Sciences* 473, 20170348.
- Liu, K., Pratapa, P.P., Misseroni, D., Tachi, T., Paulino, G.H., 2022. Triclinic metamaterials by tristable origami with reprogrammable frustration. *Advanced Materials* , 2107998.
- Liu, X., Gattas, J.M., Chen, Y., 2016. One-DOF superimposed rigid origami with multiple states. *Scientific Reports* 6, 1–9.
- McInerney, J., Paulino, G.H., Rocklin, D.Z., 2022. Discrete symmetries control geometric mechanics in parallelogram-based origami. *Proceedings of the National Academy of Sciences* 119, e2202777119.
- Miura, K., 1985. Method of packaging and deployment of large membranes in space. *The Institute of Space and Astronautical Science Report* 618, 1–9.
- Mu, J., Hou, C., Wang, H., Li, Y., Zhang, Q., Zhu, M., 2015. Origami-inspired active graphene-based paper for programmable instant self-folding walking devices. *Science Advances* 1, e1500533.
- Nassar, H., Lebée, A., Monasse, L., 2017. Curvature, metric and parametrization of origami tessellations: theory and application to the eggbox pattern. *Proceedings of the Royal Society - A* 473, 20160705.
- Nassar, H., Lebée, A., Werner, E., 2022. Strain compatibility and gradient elasticity in morphing origami metamaterials. *Extreme Mechanics Letters* 53, 101722.
- Park, S., Gao, X., 2006. Bernoulli–euler beam model based on a modified couple stress theory. *Journal of Micromechanics and Microengineering* 16, 2355.
- Pratapa, P.P., Liu, K., Paulino, G.H., 2019. Geometric mechanics of origami patterns exhibiting Poisson’s ratio switch by breaking mountain and valley assignment. *Physical Review Letters* 122, 155501.
- Pratapa, P.P., Liu, K., Vasudevan, S.P., Paulino, G.H., 2021. Reprogrammable kinematic branches in tessellated origami structures. *Journal of Mechanisms and Robotics* 13, 031102.
- Reddy, J.N., 2013. *An introduction to continuum mechanics*. Cambridge University Press.
- Schenk, M., 2012. *Folded shell structures*. Ph.D. thesis. University of Cambridge.
- Schenk, M., Guest, S.D., 2011. Origami folding: A structural engineering approach, in: *Origami5: Proceedings of the Fifth International Meeting on Origami Science, Mathematics, and Education*, CRC Press, Boca Raton, FL. pp. 291–304.
- Schenk, M., Guest, S.D., 2013. Geometry of Miura-folded metamaterials. *Proceedings of the National Academy of Sciences* 110, 3276–3281.
- Seffen, K.A., 2012. Compliant shell mechanisms. *Philosophical Transactions of the Royal Society A: Mathematical, Physical and Engineering Sciences* 370, 2010–2026.
- Silverberg, J.L., Evans, A.A., McLeod, L., Hayward, R.C., Hull, T., Santangelo, C.D., Cohen, I., 2014. Using origami design principles to fold reprogrammable mechanical metamaterials. *Science* 345, 647–650.

- Srinivasa, A.R., Reddy, J., 2017. An overview of theories of continuum mechanics with nonlocal elastic response and a general framework for conservative and dissipative systems. *Applied Mechanics Reviews* 69.
- Thai, H.T., Kim, S.E., 2015. A review of theories for the modeling and analysis of functionally graded plates and shells. *Composite Structures* 128, 70–86.
- Thai, H.T., Vo, T.P., Nguyen, T.K., Kim, S.E., 2017. A review of continuum mechanics models for size-dependent analysis of beams and plates. *Composite Structures* 177, 196–219.
- Tilley, R.J., 2020. *Crystals and crystal structures*. John Wiley & Sons.
- Toupin, R., 1962. Elastic materials with couple-stresses. *Archive for Rational Mechanics and Analysis* 11, 385–414.
- Vasudevan, S.P., Pratapa, P.P., 2021. Origami metamaterials with near-constant poisson functions over finite strains. *Journal of Engineering Mechanics* 147, 04021093.
- Vigliotti, A., Pasini, D., 2012. Linear multiscale analysis and finite element validation of stretching and bending dominated lattice materials. *Mechanics of Materials* 46, 57–68.
- Wei, Z.Y., Guo, Z.V., Dudte, L., Liang, H.Y., Mahadevan, L., 2013. Geometric mechanics of periodic pleated origami. *Physical Review Letters* 110, 215501.
- Zhang, D.G., Zhou, Y.H., 2008. A theoretical analysis of fgm thin plates based on physical neutral surface. *Computational Materials Science* 44, 716–720.
- Zhu, Y., Schenk, M., Filipov, E.T., 2022. A review on origami simulations: From kinematics, to mechanics, toward multiphysics. *Applied Mechanics Reviews* 74, 030801.
- Zirbel, S.A., Lang, R.J., Thomson, M.W., Sigel, D.A., Walkemeyer, P.E., Trease, B.P., Magleby, S.P., Howell, L.L., 2013. Accommodating thickness in origami-based deployable arrays. *Journal of Mechanical Design* 135.

# Supplementary Material for “Homogenization of non-rigid origami metamaterials as Kirchhoff-Love plates”

Siva P. Vasudevan and Phanisri P. Pratapa

Department of Civil Engineering, Indian Institute of Technology Madras, Chennai, TN 600036, India

Email: ppratapa@civil.iitm.ac.in

## S1 Macroscopic deformation field in periodic lattices

In homogenization theory, lattice dimensions are typically much larger than the unit cell. In such large (infinite) lattices, two scales of deformation are considered: one that is uniform at the global scale and another that occurs within a unit cell [Hassani and Hinton, 1998]. Here, we denote the first type of deformation, corresponding to the global scale, as the macroscopic deformation field. To illustrate this, let’s consider a portion of an infinite lattice with lattice points having sinusoidal distribution, as depicted in Fig. S1a. In the deformed state, the lattice points within each unit cell may exhibit complex configurations, as shown in Fig. S1b. Nonetheless, at the global scale, we observe a uniform expansion across the lattice, which we term the macroscopic deformation (in this case, strain) field.

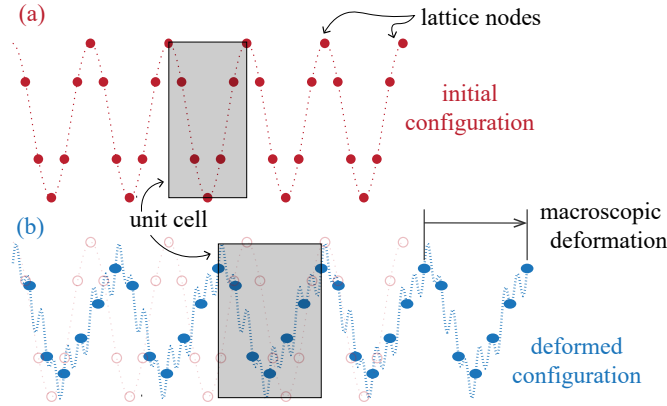


Figure S1: Illustration of a macroscopic deformation field in a periodic lattice. Under a uniform strain field, the nodes deform from the initial configuration shown in (a) to a deformed configuration shown in (b). The global field induces a homogeneous or periodic deformation across the lattice with a wavelength equal to the lattice vector.

## S2 Stiffness matrix of the 1D zigzag unit cell

This section provides the calculations of stiffness matrix  $\mathbf{K}$  for the unit cell of the 1D zigzag lattice.

We define the geometry of the zigzag unit cell by introducing vectors along the bars (see Fig. S2). Let the  $i^{\text{th}}$  bar vector be  $\mathbf{l}_i$  and the angle subtended by it with the vertical be  $\gamma_i$  for  $i \in \{1, 2, 3\}$ . Let the two translational *dofs* at the  $j^{\text{th}}$  node, located at  $(x_j, z_j)$ , be  $q_{2j-1}$  and  $q_{2j}$  for  $j \in \{1, 2, 3, 4\}$ .

The stiffness matrix of the compliant foldable system is obtained as a combination of the stiffness contribution from bars and the hinges (rotational springs at nodes). We estimate these contributions below.

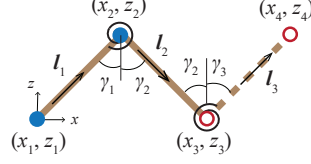


Figure S2: Unit cell of 1D zigzag lattice.

## S2.1 Contribution of bar stiffness

Let  $l_i$  denote the magnitude of  $\mathbf{l}_i$ . Then, from geometry, the elongations  $dl_i$  of  $i^{\text{th}}$  bar is related to the displacements  $(u_{ix}, u_{iz})$  and  $(u_{(i+1)x}, u_{(i+1)z})$  of the connecting nodes as

$$dl_i = [u_{(i+1)x} \sin \gamma_i + (-1)^{i+1} u_{(i+1)z} \cos \gamma_i] - [u_{ix} \sin \gamma_i + (-1)^{i+1} u_{iz} \cos \gamma_i]. \quad (1)$$

We write the above expression in terms of the perturbations of nodal *dofs* as

$$dl_i = [dq_{2i+1} \sin \gamma_i + (-1)^{i+1} dq_{2i+2} \cos \gamma_i] - [dq_{2i-1} \sin \gamma_i + (-1)^{i+1} dq_{2i} \cos \gamma_i]. \quad (2)$$

Next, the components of the compatibility matrix  $\mathbf{B}_{bar[3 \times 8]}$  is determined as the partial derivative of the  $i^{\text{th}}$  bar length  $l_i$  with  $k^{\text{th}}$  *dofs*  $q_k$ , for  $1 \leq i \leq 3$  and  $1 \leq k \leq 8$ :

$$\begin{aligned} (B_{bar})_{ik} &= \frac{\partial l_i}{\partial q_k} \\ &= (2i+1, k) \sin \gamma_i + (-1)^{i+1} (2i+2, k) \cos \gamma_i - (2i-1, k) \sin \gamma_i + (-1)^i (2i, k) \cos \gamma_i, \end{aligned} \quad (3)$$

where  $(m, n) = 1$  if  $m = n$ , and 0 for other  $m, n \in \mathbb{Z}$ . Finally, the contribution of the bar stiffness  $\mathbf{K}_{bar}$  to the global stiffness matrix is found as

$$\mathbf{K}_{bar} = \mathbf{B}_{bar}^T \mathbf{k}_{bar} \mathbf{B}_{bar}, \quad (4)$$

where  $\mathbf{k}_{bar}$  is the collection of the local axial stiffness  $k_{is}$  of the  $i^{\text{th}}$  bar  $\forall i \in \{1, 2, 3\}$ :

$$\mathbf{k}_{bar} = \begin{bmatrix} k_{1s} & 0 & 0 \\ 0 & k_{2s} & 0 \\ 0 & 0 & k_{3s} \end{bmatrix}. \quad (5)$$

For the special case of  $l_i = l$ ,  $k_{1s} = k_{2s} = k_s$ ,  $k_{3s} = 0$ ,  $\gamma_i = \gamma$ ,  $\mathbf{K}_{bar}$  becomes

$$\mathbf{K}_{bar} = k_s \begin{bmatrix} s_\gamma^2 & c_\gamma s_\gamma & -s_\gamma^2 & -c_\gamma s_\gamma & 0 & 0 & 0 & 0 \\ c_\gamma s_\gamma & c_\gamma^2 & -c_\gamma s_\gamma & -c_\gamma^2 & 0 & 0 & 0 & 0 \\ -s_\gamma^2 & -c_\gamma s_\gamma & 2s_\gamma^2 & 0 & -s_\gamma^2 & c_\gamma s_\gamma & 0 & 0 \\ -c_\gamma s_\gamma & -c_\gamma^2 & 0 & 2c_\gamma^2 & c_\gamma s_\gamma & -c_\gamma^2 & 0 & 0 \\ 0 & 0 & -s_\gamma^2 & c_\gamma s_\gamma & s_\gamma^2 & -c_\gamma s_\gamma & 0 & 0 \\ 0 & 0 & c_\gamma s_\gamma & -c_\gamma^2 & -c_\gamma s_\gamma & c_\gamma^2 & 0 & 0 \\ 0 & 0 & 0 & 0 & 0 & 0 & 0 & 0 \\ 0 & 0 & 0 & 0 & 0 & 0 & 0 & 0 \end{bmatrix}, \quad (6)$$

where  $s_\gamma \equiv \sin \gamma$  and  $c_\gamma \equiv \cos \gamma$ .

## S2.2 Contribution of rotational hinge stiffness

Let the angle between  $i^{\text{th}}$  and  $(i+1)^{\text{th}}$  bars be  $\rho_i$ :

$$\rho_i = \gamma_i + \gamma_{i+1}. \quad (7)$$

By taking inner product  $(\cdot)$  of bar vectors  $\mathbf{l}_i$  and  $\mathbf{l}_{i+1}$ , we get

$$\cos \rho_i = -\frac{\mathbf{l}_i \cdot \mathbf{l}_{i+1}}{l_i l_{i+1}}. \quad (8)$$

By partially differentiating the above equation with  $k^{\text{th}}$  dofs  $q_k$  we get the compatibility matrix  $\mathbf{B}_{hinge[2 \times 8]}$ :

$$\begin{aligned} (B_{hinge})_{ik} &= \frac{\partial \rho_i}{\partial q_k} \\ &= \frac{1}{l_i l_{i+1} \sin \rho_i} \left[ \left( \mathbf{l}_i + \frac{l_i}{l_{i+1}} \cos \rho_i \mathbf{l}_{i+1} \right) \cdot \frac{\partial \mathbf{l}_{i+1}}{\partial q_k} + \left( \mathbf{l}_{i+1} + \frac{l_{i+1}}{l_i} \cos \rho_i \mathbf{l}_i \right) \cdot \frac{\partial \mathbf{l}_i}{\partial q_k} \right]. \end{aligned} \quad (9)$$

In the above equation, we use the definition of bar vector  $\mathbf{l}_i$  as a function of the nodal coordinates (and the dofs) to find the partial derivative of  $\mathbf{l}_i$  with  $q_k$ :

$$\mathbf{l}_i = \begin{bmatrix} x_{i+1} - x_i \\ z_{i+1} - z_i \end{bmatrix} = \begin{bmatrix} q_{2i+1} - q_{2i-1} \\ q_{2i+2} - q_{2i} \end{bmatrix}. \quad (10)$$

Partially differentiating this equation, we find:

$$\frac{\partial \mathbf{l}_i}{\partial q_k} = \begin{bmatrix} (2i+1, k) - (2i-1, k) \\ (2i+2, k) - (2i, k) \end{bmatrix}, \quad (11)$$

where  $(m, n) = 1$  if  $m = n$ , and 0 for other  $m, n \in \mathbb{Z}$ . Next, the contribution of the hinge stiffness  $\mathbf{K}_{hinge}$  to the global stiffness matrix is found as

$$\mathbf{K}_{hinge} = \mathbf{B}_{hinge}^T \mathbf{k}_{hinge} \mathbf{B}_{hinge}, \quad (12)$$

where  $\mathbf{k}_{hinge}$  is the collection of the local hinge stiffness  $k_{ih}$  of  $i^{\text{th}}$  hinge  $\forall i \in \{1, 2\}$ :

$$\mathbf{k}_{hinge} = \begin{bmatrix} k_{1h} & 0 \\ 0 & k_{2h} \end{bmatrix}. \quad (13)$$

For the special case of  $l_i = l$ ,  $k_{1h} = k_{2h} = k_h$ ,  $\gamma_i = \gamma$ ,  $\mathbf{K}_{hinge}$  becomes

$$\mathbf{K}_{hinge} = \frac{k_h}{l^2} \begin{bmatrix} c_\gamma^2 & -s_\gamma c_\gamma & 0 & 2s_\gamma c_\gamma & -c_\gamma^2 & -s_\gamma c_\gamma & 0 & 0 \\ -s_\gamma c_\gamma & s_\gamma^2 & 0 & -2s_\gamma^2 & s_\gamma c_\gamma & s_\gamma^2 & 0 & 0 \\ 0 & 0 & c_\gamma^2 & s_\gamma c_\gamma & 0 & -2s_\gamma c_\gamma & -c_\gamma^2 & s_\gamma c_\gamma \\ 2s_\gamma c_\gamma & -2s_\gamma^2 & s_\gamma c_\gamma & 5s_\gamma^2 & -2s_\gamma c_\gamma & -4s_\gamma^2 & -s_\gamma c_\gamma & s_\gamma^2 \\ -c_\gamma^2 & s_\gamma c_\gamma & 0 & -2s_\gamma c_\gamma & c_\gamma^2 & s_\gamma c_\gamma & 0 & 0 \\ -s_\gamma c_\gamma & s_\gamma^2 & -2s_\gamma c_\gamma & -4s_\gamma^2 & s_\gamma c_\gamma & 5s_\gamma^2 & 2s_\gamma c_\gamma & -2s_\gamma^2 \\ 0 & 0 & -c_\gamma^2 & -2s_\gamma c_\gamma & 0 & 2s_\gamma c_\gamma & c_\gamma^2 & -s_\gamma c_\gamma \\ 0 & 0 & s_\gamma c_\gamma & s_\gamma^2 & 0 & -2s_\gamma^2 & -s_\gamma c_\gamma & s_\gamma^2 \end{bmatrix}, \quad (14)$$

where  $s_\gamma \equiv \sin \gamma$  and  $c_\gamma \equiv \cos \gamma$ .

### S2.3 Global stiffness matrix

Finally, we express the global stiffness matrix  $\mathbf{K}$  as the sum of contributions from the bar and hinge stiffness in Eqns. 6 and 14:

$$\mathbf{K} = \mathbf{K}_{bar} + \mathbf{K}_{hinge}. \quad (15)$$

For these numerical values:  $\gamma = 90^\circ - \theta = 45^\circ$ ,  $l = 50$ ,  $k_s = 100$  and  $k_h = 1$ ,  $\mathbf{K}$  becomes

$$\mathbf{K} = \begin{bmatrix} 50 + \phi & 50 - \phi & -50 & -50 + 2\phi & -\phi & -\phi & 0 & 0 \\ 50 - \phi & 50 + \phi & -50 & -50 - 2\phi & 0 + \phi & 0 + \phi & 0 & 0 \\ -50 & -50 & 100 + \phi & 0 + \phi & -50 & 50 - 2\phi & -\phi & \phi \\ -50 + 2\phi & -50 - 2\phi & \phi & 100 + 5\phi & 50 - 2\phi & -50 - 4\phi & -\phi & \phi \\ -\phi & \phi & -50 & 50 - 2\phi & 50 + \phi & -50 + \phi & 0 & 0 \\ -\phi & \phi & 50 - 2\phi & -50 - 4\phi & -50 + \phi & 50 + 5\phi & 2\phi & -2\phi \\ 0 & 0 & -\phi & -0 + \phi & 0 & 2\phi & \phi & -\phi \\ 0 & 0 & \phi & \phi & 0 & -2\phi & -\phi & \phi \end{bmatrix}, \quad (16)$$

where  $\phi = (k_h \sin^2 \gamma)/l^2 = 0.0002$ .

### S3 Details on convergence studies

This section discusses convergence studies for numerical simulations with the Bar-and-Hinge (BnH) and Finite Element Methods (FEM). Initially, we fix the cell count in the lattice by doing a convergence study with the BnH method, then we use that count to model the lattice with FEM to investigate the effect of mesh size. Finally, we validate the homogenized elastic constants by comparing them with BnH and FEM results.

#### S3.1 Convergence study in the bar-and-hinge model

In Section 4.2 of the main paper, we discussed the validation of homogenized results via numerical simulations of a finite lattice using the BnH method. In this section, we explain the rationale behind selecting the number of cells through a convergence study. The variation of Young’s modulus  $E_x$  with the number of cells (along each lattice direction) is illustrated in Fig. S3a. The convergence plot reveals that  $16 \times 16$  cells result in approximately a 1.1% error in  $E_x$  compared to the value obtained with  $32 \times 32$  cells. This convergence rate is similar for other elastic constants (excluding  $G_{xy}$ ). Consequently, for numerical simulations, we opt for a slightly higher number of cells, specifically  $20 \times 20$ , to approximate these elastic constants at the homogeneous limit with sufficient accuracy. Regarding the shear modulus  $G_{xy}$ , the number of cells converges to a different value, specifically  $4 \times 50$ . This choice promotes the extremely stiff shear mode rather than a more flexible non-homogeneous in-plane bending mode, as shown in Fig. 12c of the main paper.

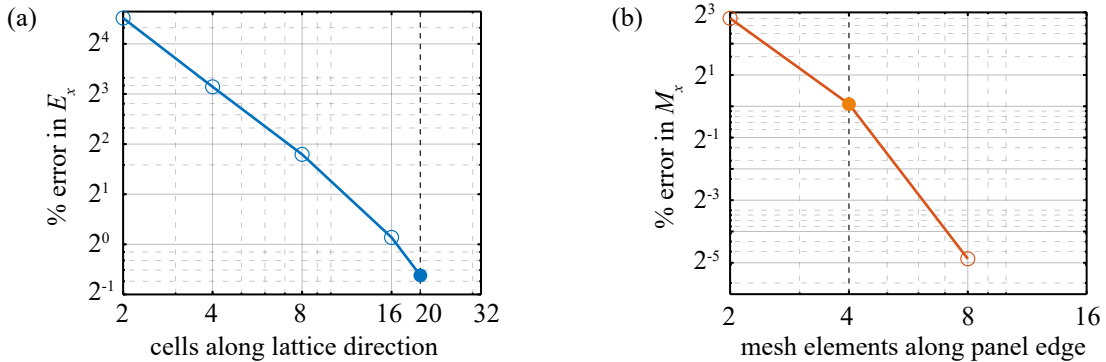


Figure S3: (a) Convergence of percentage error in  $E_x$  (relative to the value obtained from  $32 \times 32$  cells) with number of cells along each lattice direction used in BnH model. (b) Convergence of percentage error in  $M_x$  (relative to the value obtained from  $16 \times 16$  mesh elements) with number of mesh elements along the panel edges in FEM model.

#### S3.2 Convergence study in the finite element model

In addition to the BnH analysis, we perform a FEM analysis of the Miura-ori lattice to validate the homogenized results. The number of cells in the FEM model remains consistent with the BnH model. In the FEM model, the panels of the Miura-ori lattice are represented using 3D, 4-noded, quadrilateral, stress/displacement shell elements (S4R) with specified Young’s modulus  $E^{FEM}$  and thickness  $t^{FEM}$ . The creases are idealized as line hinges with a particular rotational stiffness  $k_f^{FEM}$ . We fine tune the numerical values of these three FEM parameters:  $k_f^{FEM}$ ,  $t^{FEM}$ , and  $E^{FEM}$ , with the associated BnH parameters,  $k_f$ ,  $k_b$ , and  $k_a$  to enable a fair comparison between the two models. The values of these parameters are listed in Table S1. Further, we assign a Poisson’s ratio of 0.3 to the shell material.

We note that BnH models are simplified, reduced-order parameterized models designed to capture the first order response of origami structures concerning in-plane stretching and out-of-plane bending deformations [Filipov et al., 2017], which are also the modes of interest in this study. When panel elongations are

negligible, BnH and FEM models yield comparable results for lattice’s stretching moduli  $E_x$ ,  $E_y$  and in-plane Poisson’s ratios  $\nu_{xy}^s$ ,  $\nu_{yx}^s$ , provided that  $k_f = k_f^{FEM}$ . By appropriately adjusting the shell element thickness ( $t^{FEM} = t_{bend}^{FEM}$ ) in the FEM model, consistent results are achieved between BnH and FEM models for the bending moduli. Furthermore, by tuning the Young’s modulus of the shell element ( $E^{FEM}$ ) in the FEM model, we obtain similar estimates for the shear modulus from both BnH and FEM models. To establish a connection for the twisting modulus obtained from both models, it is necessary to re-adjust the shell element thickness ( $t^{FEM} = t_{twist}^{FEM}$ ) in the FEM model, as the basic BnH model was originally intended to mimic only in-plane stretching and out-of-plane bending deformations. It is important to note that the proposed homogenization framework is versatile and can be applied to other structural models estimating the stiffness matrix  $\mathbf{K}$  of origami unit cells, including FEM and higher order BnH models. However, for the sake of simplicity and to illustrate the concept, we have opted to demonstrate it using the basic BnH model. The chosen values of the FEM parameters along with the corresponding BnH parameters are detailed in Table S1.

Table S1: Numerical values of FEM and BnH parameters.

FEM	$k_f^{FEM} = 0.1\text{Nmm/rad}$ , $t_{bend}^{FEM} = 11.35\mu\text{m}$ , $t_{twist}^{FEM} = 4.1\mu\text{m}$ , $E^{FEM} = 2 \times 10^8\text{N/mm}^2$		
BnH	$k_f = 0.1\text{ Nmm/rad}$ ,	$k_b = 1\text{ Nmm/rad}$ ,	$k_a = 3.75 \times 10^7\text{ N}$

With the chosen parametric values, we do a mesh-independency study on the FEM model. Effect of number of mesh elements along each panel direction is illustrated for the bending modulus  $M_x$  in Fig. S3b. From the convergence plot, we observe that a  $4 \times 4$  mesh incurs about 1% error in  $M_x$ , relative to the value obtained from a  $16 \times 16$  mesh. A similar trend is observed for other elastic constants (excluding  $G_{xy}$ ). Consequently, we restrict to a  $4 \times 4$  mesh to estimate the elastic constants with sufficient accuracy, in view of higher computational cost involved with a finer mesh. For the pure shear test, we observe that a finer mesh with  $16 \times 16$  discretization is required to get a similar convergence rate as the panels undergo significant elongations in this mode.

### S3.3 Comparison of results from FEM and BnH models

Using the parameters provided in Table S1, we conduct all six numerical tests on a finite Miura-ori lattice (a procedure discussed in Section 4.2 of the main paper) using both FEM and BnH models. The unit cell dimensions are set to  $a = 40\text{mm}$ ,  $b = 40\text{mm}$ ,  $\alpha = 60^\circ$  and  $\theta = 60^\circ$ . These dimensions, as well as the number of cells, loading conditions, and boundary conditions, are kept consistent between both models. Strains or curvatures are calculated at an internal cell using the finite difference method under the applied loads, while force (or couple) stresses are determined as area-distributed forces (or moments). The effective elastic constants obtained from these models, and the homogenized values from the proposed framework, are presented in Table S2.

Table S2: Comparison of effective elasticity constants obtained from FEM, BnH and homogenization methods.

$E_x a^3/k_f$	$E_y a^3/k_f$	$G_{xy} a^3/k_f$	$M_x a/k_f$	$M_y a/k_f$	$T_{xy} a/k_f$	$\nu_{xy}^s$	$\nu_{yx}^s$	$\nu_{xy}^b$	$\nu_{yx}^b$
Values from BnH model									
28.47	51.33	$4.03 \times 10^9$	24.29	49.58	8.70	-1.33	-0.75	1.32	0.76
Values from FEM model									
28.19	49.22	$4.17 \times 10^9$	24.64	46.94	8.93	-1.33	-0.75	1.33	0.75
Homogenized values from proposed framework									
29.00	51.55	$4.19 \times 10^9$	25.44	45.23	8.47	-1.33	-0.75	1.33	0.75
Percentage difference between values from homogenization and FEM model									
2.9%	4.7%	0.5%	3.2%	3.6%	5.2%	0.0%	0.0%	0.0%	0.0%

We can observe from Table S2 that the values obtained through homogenization closely match those from the FEM model, with an acceptable level of accuracy (less than about 5% error), thereby validating the framework proposed in the paper. The errors obtained in the results could be further reduced by selecting a finer mesh and a greater number of cells, though this would come at the cost of increased computational time. It is crucial to emphasize that the proposed homogenization framework remains unaffected by the limitations of the structural model used to derive the stiffness matrix  $\mathbf{K}$  of the unit cell. A more detailed FEM model, for instance, could be employed to obtain the  $\mathbf{K}$  matrix of the unit cell, and the homogenization process can be applied in the same manner, as demonstrated in the manuscript, to yield a more accurate estimation of the lattice’s effective properties. This study’s scope is primarily to introduce the homogenization framework for origami lattices, and the basic BnH model was chosen for structural analysis solely for the sake of simplifying the framework’s illustration. Any alternative structural model could be used in its place.

## S4 Effective elastic constants of a physical Miura-ori prototype

In Table 3 and 4 of the main paper, we presented the effective elastic constants of the centrosymmetric and non-centrosymmetric Miura-ori lattice in a normalized form with respect to the panel edge length  $a$  and folding stiffness  $k_f$ . To provide physical interpretations of these parameters for tessellations made from real materials, we consider a paper prototype (Fig. S4) of the Miura-ori pattern with the following dimensions: panel edge lengths  $a = b = 25$  mm, paper thickness  $t = 0.3$  mm, panel angle  $\alpha = 60^\circ$ , and a folded state with  $\theta = 45^\circ$ . The material properties of the paper are taken as follows: Young’s modulus  $E_{paper} = 4000\text{N/mm}^2$ ,

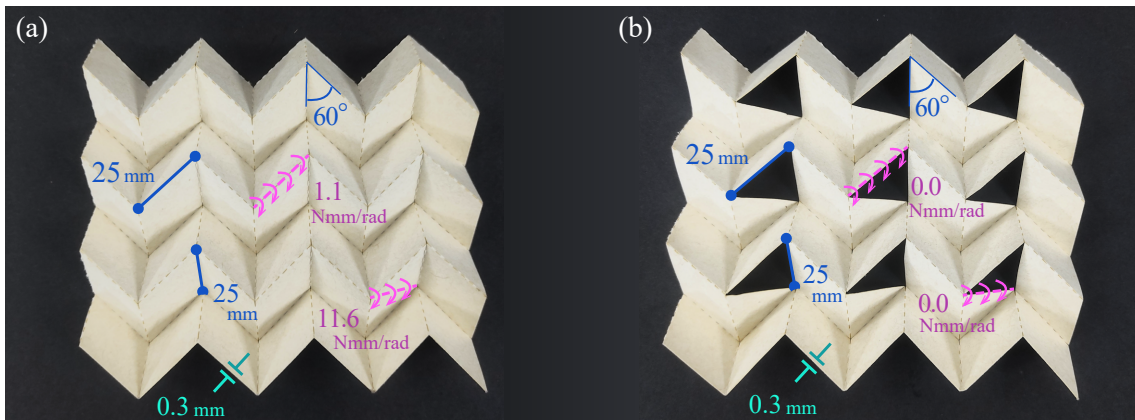


Figure S4: Dimensions and stiffness of a Miura prototype folded from paper. (a) Original pattern that is centrosymmetric. (b) Modified non-centrosymmetric pattern.

Poisson’s ratio  $\nu_{paper} = 0.3$ , and folding stiffness  $k_f = 1.1$  Nmm/rad. These material property values for paper are based on previous studies [Szewczyk, 2008, Lechenault et al., 2014]. For the taken dimensions and material, the panel bending stiffness (used in the bar-and-hinge model) is estimated as  $k_b = 11.6$ , as per Eqn. 9 in [Filipov et al., 2017]. These numerical values are summarized in Table S3 for quick reference.

Table S3: Geometric and material parameters of an origami prototype folded from a paper sheet.

$a$	$b$	$t_{paper}$	$\alpha$	$\theta$	$E_{paper}$	$\nu_{paper}$	$k_f$	$k_b$
25mm	25mm	0.3mm	$60^\circ$	$45^\circ$	4000 N/mm <sup>2</sup>	0.3	1.1 Nmm/rad	11.6 Nmm/rad

It is worth noting that the value of  $k_b = 11.6$  is approximately one order of magnitude higher than  $k_f = 1.1$  for a typical paper prototype. This is consistent with the value  $k_b/k_f = 10$  provided in Table 2 of the main paper. This table is repeated here for quick reference (Table S4).

The axial rigidity of the paper panel is of the order of  $E_{paper} \times a \times t_{paper} = 3 \times 10^4\text{N}$ . However, we choose the bar stiffness  $k_a = 10^{10}k_f/a$  to be very high to approximate rigid triangulated behavior. The bar-and-hinge parameters corresponding to the Miura-ori prototype are summarized in Table S5.

Table S4: Geometric and stiffness parameters chosen for modeling the Miura-ori cell.

$b(\text{mm})/a(\text{mm})$	$\alpha(\text{deg})$	$\theta(\text{deg})$	$k_b(\text{Nmm})/k_f(\text{Nmm})$	$k_a(\text{N})a(\text{mm})/k_f(\text{Nmm})$
1	$60^\circ$	$45^\circ$	10	$10^{10}$

Table S5: Bar-and-hinge parameters of the Miura-ori prototype.

$a$	$b$	$\alpha$	$\theta$	$k_f$	$k_b$	$k_a$
25 mm	25 mm	$60^\circ$	$45^\circ$	1.16 Nmm/rad	11.6 Nmm/rad	$4.6 \times 10^8$ N/mm

Using these parameter values, we calculate the elastic constants for the centrosymmetric (Fig. S4a) and non-centrosymmetric (Fig. S4b) Miura-ori prototypes and list them in Table S6 and Table S7, respectively. As expected, the stiffness against folding, bending, and twisting of the paper prototype are very low, comparable to that of certain soft foams and biological tissues.

Table S6: Estimated effective metamaterial constants for the centrosymmetric Miura-ori paper prototype.

$E_x$	$E_y$	$G_{xy}$	$M_x$	$M_y$	$T_{xy}$	$\nu_{xy}^s$	$\nu_{yx}^s$	$\nu_{xy}^b$	$\nu_{yx}^b$
8116.7N/m <sup>2</sup>	3607.32N/m <sup>2</sup>	$3.7 \times 10^{11}$ N/m <sup>2</sup>	2.05N	0.91N	0.34N	-1.50	-0.67	1.50	0.67

Table S7: Estimated effective metamaterial constants for the non-centrosymmetric Miura-ori paper prototype.

$E_x$	$E_y$	$G_{xy}$	$M_x$	$M_y$	$T_{xy}$	$\nu_{xy}^s$	$\nu_{yx}^s$	$\nu_{xy}^b$	$\nu_{yx}^b$
6026.80N/m <sup>2</sup>	2678.58N/m <sup>2</sup>	$3 \times 10^{11}$ N/m <sup>2</sup>	1.40N	0.62N	0.23N	-1.50	-0.67	1.50	0.67

## References

- [Filipov et al., 2017] Filipov, E. T., Liu, K., Tachi, T., Schenk, M., and Paulino, G. H. (2017). Bar and hinge models for scalable analysis of origami. *International Journal of Solids and Structures*, 124:26–45.
- [Hassani and Hinton, 1998] Hassani, B. and Hinton, E. (1998). A review of homogenization and topology optimization i—homogenization theory for media with periodic structure. *Computers & Structures*, 69(6):707–717.
- [Lechenault et al., 2014] Lechenault, F., Thiria, B., and Adda-Bedia, M. (2014). Mechanical response of a creased sheet. *Physical Review Letters*, 112(24):244301.
- [Szewczyk, 2008] Szewczyk, W. (2008). Determination of Poisson’s ratio in the plane of the paper. *Fibres & Textiles in Eastern Europe*, 4:117–120.